

AD-A241 514



AEOSR-TR- 91 0787

2

FINAL TECHNICAL REPORT
TO
AIR FORCE OFFICE OF SCIENTIFIC RESEARCH
HYPERVELOCITY AERODYNAMICS AND CONTROL

AFOSR Contract No. F49620-86-C-0138

September 15, 1986 to October 14, 1987

DTIC
S E L E C T E D
OCT 10 1991
D

Principal Investigators
T. C. Adamson, Jr. and R. M. Howe
Department of Aerospace Engineering
The University of Michigan

December 1987

Approved for Public Release, Distribution Unlimited
Reproduction in Whole or Part is Permitted for any
Purpose of the United States Government

91-13028



91 1010 039

REPORT DOCUMENTATION PAGE

1a. REPORT SECURITY CLASSIFICATION Unclassified		1b. RESTRICTIVE MARKINGS	
2a. SECURITY CLASSIFICATION AUTHORITY		3. DISTRIBUTION/AVAILABILITY OF REPORT <i>unlimited</i>	
2b. DECLASSIFICATION/DOWNGRADING SCHEDULE			
4. PERFORMING ORGANIZATION REPORT NUMBER(S) Final Technical Report		5. MONITORING ORGANIZATION REPORT NUMBER(S)	
6a. NAME OF PERFORMING ORGANIZATION Dept of Aerospace Engineering The University of Michigan		7a. NAME OF MONITORING ORGANIZATION AFOSR	
6c. ADDRESS (City, State and ZIP Code) Ann Arbor, MI 48109-2140		7c. ADDRESS (City, State and ZIP Code) Bolling AFB, DC 20332-6448	
8a. NAME OF FUNDING/SPONSORING ORGANIZATION <i>Same as 7A</i>		9. PROCUREMENT INSTRUMENT IDENTIFICATION NUMBER AFOSR Contract No. F 49620-86-C-0138	
8c. ADDRESS (City, State and ZIP Code) <i>Same As 7b</i>		10. SOURCE OF FUNDING NOS.	
		PROGRAM ELEMENT NO. <i>623224</i>	PROJECT NO. <i>SD1</i>
		TASK NO. <i>00</i>	WORK UNIT NO.
11. TITLE (Include Security Classification) Hypervelocity Aerodynamics and Control			
12. PERSONAL AUTHOR(S) Prof. T. C. Adamson, Jr., Prof. R. M. Howe			
13a. TYPE OF REPORT Final Technical	13b. TIME COVERED FROM 9/15/86 TO 10/14/87	14. DATE OF REPORT (Yr., Mo., Day) December 1987	15. PAGE COUNT
16. SUPPLEMENTARY NOTATION			
17. COSATI CODES		18. SUBJECT TERMS (Continue on reverse if necessary and identify by block number)	
FIELD	GROUP	SUB GR.	
		Optimal Trajectory	
		Supercircular Speeds	
		Optimal Control	
		Hypersonic Flow	
		Gas Injection	
		Numerical Methods	
19. ABSTRACT (Continue on reverse if necessary and identify by block number) A study of optimal aerodynamics and propulsive control at supersonic speeds has been initiated. The objective of the research is to develop methods for determining optimal guidance and control of earth launch kinetic energy weapons designed to intercept intercontinental ballistic missiles early in their ascent trajectory. Optimal control techniques are being used to obtain multi-stage trajectories based on minimizing the mass ratio. Study parameters include time of flight, down range intercept distance and intercept altitude. Re-entry/skip trajectories are considered. Innovative means of attitude control of the final stage which intercepts the target are being studied. In addition an investigation of the control of aerodynamic forces on hypersonic vehicles by boundary layer injection has been started. The goal of this work is to determine optimal patterns of injection of a gas into a boundary layer on a hypersonic vehicle, to generate desired aerodynamic forces. Two directions of approach are being studied. In the first, analytical means are			
20. DISTRIBUTION/AVAILABILITY OF ABSTRACT UNCLASSIFIED/UNLIMITED <input checked="" type="checkbox"/> SAME AS RPT. <input type="checkbox"/> DTIC USERS <input type="checkbox"/>		21. ABSTRACT SECURITY CLASSIFICATION <i>unclassified</i>	
22a. NAME OF RESPONSIBLE INDIVIDUAL <i>Barker</i>		22b. TELEPHONE NUMBER (Include Area Code) <i>202-767-5011</i>	22c. OFFICE SYMBOL <i>NP</i>

SECURITY CLASSIFICATION OF THIS PAGE

being used to study the effects of blowing on simple flow problems in the various flow regimes; a combination of asymptotic and numerical methods are in use. In the second, numerical methods are being used, with particular emphasis on obtaining efficient codes which result in the computation of crisp shock waves and which can handle blowing in the boundary layer. Both distributed and strip blowing are under consideration.

I. Summary

A study of optimal aerodynamics and propulsive control at supercircular speeds has been initiated. The objective of the research is to develop methods for determining optimal guidance and control of earth launch kinetic energy weapons designed to intercept intercontinental ballistic missiles early in their ascent trajectory. Optimal control techniques are being used to obtain multi-stage trajectories based on minimizing the mass ratio. Study parameters include time of flight, down range intercept distance and intercept altitude. Re-entry/skip trajectories are considered. Innovative means of attitude control of the final stage which intercepts the target are being studied.

In addition an investigation of the control of aerodynamic forces on hypersonic vehicles by boundary layer injection has been started. The goal of this work is to determine optimal patterns of injection of a gas into a boundary layer on a hypersonic vehicle, to generate desired aerodynamic forces. Two directions of approach are being studied. In the first, analytical means are being used to study the effects of blowing on simple flow problems in the various flow regimes; a combination of asymptotic and numerical methods are in use. In the second, numerical methods are being used, with particular emphasis on obtaining efficient codes which result in the computation of crisp shock waves and which can handle blowing in the boundary layer. Both distributed and strip blowing are under consideration.

Preliminary results are presented.

II. Research Objectives

The contract for this research work has two phases, one dealing with optimal trajectories at superorbital velocities and the other with aerodynamic force calculations. Hence the work statement for the year's work has two separate parts as follows, where paragraph numbering from the contract is repeated here.

0001AA

1. Formulate the automatic control problem description of the dynamics of transatmospheric vehicles for ballistic missile defense. Appropriate control laws shall be determined and techniques for vehicle optimization shall be developed.



Availability Codes	
Dist	Avail. and/or Special
A-1	

2. Examine schemes for the generation of aerodynamic control forces on hypervelocity vehicles by the injection of gas into the boundary layer. Plan analytical and numerical investigation of both slot and surface injection from hypersonic slender bodies and select techniques for distinguishing among dominant fluid mechanical phenomena. Minimize the effects of numerical difference schemes upon shock wave thickness and location.

III. Status of the Research Effort

This work began on August 15, 1986. The contract was to be for 37 months, divided into three periods, the first being 13 months and the last two being 12 months each. At the end of the first period, pending demonstration of satisfactory work, the first option was to be exercised in order that work during the second period could proceed. A technical briefing was given to Col. D. Finkleman (Air Force), Col. W. Merritt (Army) and Major S. Rezwick (Air Force) in early August of 1986; it was indicated that they were well satisfied with the technical effort and results. However, during the time that option one could have been exercised, the contract was being transferred to Army supervision and apparently the group transferring the contract to the Army was not aware that further action was required. As a result this contract is terminated after 13 months and a new contract for the remaining two options is being renegotiated with the Army Strategic Defense Command. Thus, this final report covers one year of a proposed three year effort. The following status report is in two parts, with the numbering corresponding to that of the phases in the work statement.

1. Optimal Aerodynamic and Propulsive Control of Intercept Trajectories at Supercircular Speeds.

Robert M. Howe, Principal Investigator

Nguyen X. Vinh Co-Investigator

Elmer G. Gilbert Co-Investigator

Ping Lu, Graduate Student

Aharon Karou, Visiting Scholar

Gil Shorr, Visiting Scholar

1.1 Introduction

The utilization of satellite-based kinetic-energy weapons for intercepting intercontinental ballistic missiles during their ascent trajectory constitutes one of the major efforts in the current

U.S. Strategic Defense Initiative program. In this research we have considered an alternative to space-based weapons, namely, the use of land or sea-based kinetic energy interceptors. When such interceptors are based on the U.S. continent, ranges of up to 5000 miles are needed. If the interceptors are sea launched, for example from submarines, the required interceptor range can be reduced to as little as 2000 miles or less. In either case the interceptor must accelerate to very high speeds, typically twice circular orbit velocity, in order to reach a target at these distances within several minutes.

In order to achieve these velocities, a rocket powered interceptor requires an overall mass ratio of several thousand to one. Even so, the interceptor takeoff weight can be held within reasonable bounds by the use of miniature guided warheads. It is clear that such large mass ratios can only be achieved by using between 4 and 7 rocket boost stages. In this research we have considered the problem of optimizing a number of stage parameters and the angle of attack control in order to minimize the overall required mass ratio. The time history of angle of attack was parameterized by letting the angle of attack for each thrusting stage vary linearly with time. Additional parameters to be optimized included the thrust burn times for each stage and the coast times between stage burns. Although rockets of this type would normally be launched straight up, we have also included the initial launch flight-path angle as a parameter. This was based on the assumption that a fairly rapid pitchover maneuver can be performed immediately after launch to achieve the desired initial flight path angle.

Once the trajectory optimization problem has been converted to a parameter optimization problem, a quasi-Newton minimization algorithm is utilized with penalty functions to implement the terminal constraints required for intercept, as well as any additional constraints. The necessary gradients of the cost function with respect to the parameters are computed numerically using finite differences. A complete multi-stage trajectory must be run using numerical integration for every evaluation of the cost function. For each set of N parameters this means that $N+1$ complete trajectories must be computed, one to evaluate the cost function for the given parameter settings, and N to evaluate the gradient of the cost function with respect to each of the N parameters. In the trajectory optimization problems we have considered, between 10 and 20 parameters are used. Thus between 11 and 21 complete multi-stage trajectories must be computed numerically for a single iteration of the optimization procedure. Also, each iteration utilizes a line search which requires several additional trajectory computations. It has been found that between 200 and 400 iterations are needed until satisfactory convergence to an optimal solution is achieved. It follows that several thousand trajectories must be computed for each optimization case considered. In order to reduce the overall computational time, the multiple-stage trajectories were calculated using

an AD 100 multiprocessor computer. A VAX host computer was used to implement the optimization algorithm and input new parameters to the AD 100 for each successive trajectory run. In this way the total time required for an overall trajectory optimization was reduced from several hours to several minutes.

In the next section scalar equations of motion for the interceptor trajectory are presented. Subsequent sections discuss the optimization problem, its numerical solution, and results for a typical 4-stage trajectory optimization.

1.2 Equations of Motion

In order to reduce the trajectory computation times, only the two dimensional equations of motion of the interceptor were considered. As a further simplification, the effect of earth's rotation was neglected. It was felt that neither of these simplifications altered the overall nature of the optimization problem. More comprehensive equations of motion can always be incorporated into the optimization problem at a later time to improve the accuracy for those cases which may turn out to be of practical interest. Thus the interceptor rocket was considered to be a point mass m moving in a plane which contains the center of a spherical, non-rotating earth with inverse square gravitational field. A convenient and efficient method for representing the velocity state of the interceptor is in terms of the total velocity and the flight path angle with respect to the local horizontal [1]. This leads to the following two-dimensional equations of motion:

$$\dot{r} = V \sin \gamma \quad (1.1)$$

$$\dot{\theta} = \frac{V}{r} \cos \gamma \quad (1.2)$$

$$\dot{V} = \frac{T}{m} \cos \alpha - \frac{D}{m} - \frac{g_0 r_0^2}{r^2} \sin \gamma \quad (1.3)$$

$$\dot{\gamma} = \frac{1}{V} \left[\frac{T}{m} \sin \alpha + \frac{L}{m} - \frac{g_0 r_0^2}{r^2} \cos \gamma + \frac{V^2}{r} \cos \gamma \right] \quad (1.4)$$

$$\dot{m} = \frac{T}{I_{sp} g_0} \quad (1.5)$$

where

r = radial distance from center of earth

θ = polar angle

V = total velocity

γ = flight path angle

m = interceptor mass

T = rocket thrust

α = angle of attack

D = aerodynamic drag

L = aerodynamic lift

r_0 = reference radius

g_0 = gravity acceleration at $r = r_0$

I_{sp} = specific impulse of rocket motor

The aerodynamic lift, L , and drag, D , are given by the following formulas:

$$L = \frac{1}{2} \rho V^2 A C_L, \quad D = \frac{1}{2} \rho V^2 A C_D \quad (1.6)$$

$$C_L = C_N \cos \alpha - C_A \sin \alpha, \quad C_D = C_N \sin \alpha + C_A \cos \alpha \quad (1.7)$$

where

ρ = atmospheric density

A = interceptor cross-sectional area

C_L = lift coefficient

C_D = drag coefficient

C_N = normal force coefficient

C_A = axial force coefficient

C_N and C_A , which represent aerodynamic normal and axial force coefficients in body axes, can be approximated for slender bodies by the following formulas [2]:

$$C_N = \sin 2\alpha \cos \frac{\alpha}{2} + \frac{5}{\pi} \frac{\lambda}{d} \sin \alpha |\sin \alpha|, \quad C_A = 0.15 \quad (1.8)$$

where

λ = rocket length

d = rocket diameter

The atmospheric density, ρ , in Eq. (1.6) is a function of the rocket altitude h , which is given by the equation

$$h = (R - 1) r_0 \quad (1.9)$$

Three different methods for approximating the variation of ρ with h were considered. The first utilizes table lookup with linear interpolation based on a tabulated standard atmosphere. This method introduces into the simulation a function with discontinuous slopes, which has the potential of causing numerical difficulties in the descent algorithm (see Section 1.4). The second method uses the following exponential approximation:

$$\rho = \rho_0 e^{-\beta h} \quad (1.10)$$

where $1/\beta = 23,500$ ft. and ρ_0 is the atmospheric density at sealevel. The third method uses the following analytic approximation [3]:

$$\rho/\rho_0 = [A_0 + A_1 h + A_2 h^2 + \dots + A_{11} h^{11}]^{-4} \quad (1.11)$$

with

$$\begin{aligned} A_0 &= 1.0000000000 & A_1 &= 0.3393495800 \times 10^{-1} & A_2 &= -0.3433553057 \times 10^{-2} \\ A_3 &= 0.5497466428 \times 10^{-3} & A_4 &= -0.3228358326 \times 10^{-4} & A_5 &= 0.1106617734 \times 10^{-5} \\ A_6 &= -0.2291755793 \times 10^{-7} & A_7 &= 0.2902146443 \times 10^{-9} & A_8 &= -0.2230070938 \times 10^{-11} \\ A_9 &= 0.1010575266 \times 10^{-13} & A_{10} &= -0.2482089627 \times 10^{-16} & A_{11} &= 0.2548769715 \times 10^{-19} \end{aligned}$$

Eq. (1.11) is valid from 0 to 200 km. altitude and is accurate to better than 5 percent for altitudes up to 70 km. It is a considerably better approximation than the exponential model in Eq. (1.10) and takes no longer for computer execution than the table lookup scheme. Thus it represented our preferred approach.

Dimensionless versions of Eqs. (1.1) through (1.9) and Eq. (1.11) were used for the trajectory simulation of each inteceptor stage while thrusting or coasting ($T = 0$). The state variables r , θ , V and γ are continuous from one stage to the next. On the other hand, the state variable m , which represents the mass of each stage, undergoes a discontinuous decrease each time a stage burns out and is dropped. The mass state m can be made continuous by defining it as the mass of rocket fuel divided by the initial takeoff mass. The total instantaneous mass for each stage is then the sum of the fuel mass and the inert mass. The burn time for each stage, as well as the coast time per stage, constitute parameters to be optimized. For a given stage mass ratio, the stage burn time determines the thrust level for the stage. Thus the parameters representing stage burn times are equivalent to parameters representing stage thrust levels. As noted previously, the time history of angle of attack was parameterized by letting it vary linearly for each stage. Thus an additional parameter per stage is the time-rate-of-change of angle of attack.

1.3. Constraints and Optimization Problem Formulation

To complete the statement of the optimization problem it was necessary to introduce certain constraints on the trajectory and its defining parameters. The most obvious of these were the ones required for target interception. After final stage cutoff, the payload must coast in such a manner that at the specified intercept time, t_f , the position variables, $r(t_f)$ and $\theta(t_f)$, match those of the target.

There are several ways to implement the intercept conditions. One way is to impose them at the time of final-stage cutoff, t_c . If $r(t_c)$, $\theta(t_c)$, $r(t_f)$, and $\theta(t_f)$ are known and the coast is an out-of-the-atmosphere conic transfer, the values $\gamma(t_c)$ and $V(t_c)$ required for intercept are determined by solving an appropriate Lambert problem. This can be done numerically by the methods given in [4]. The errors between the required and actual values of $\gamma(t_c)$ and $V(t_c)$ must be zero for intercept and these conditions give two equality constraints on the trajectory at $t = t_c$.

It was found that unconstrained optimal conic coast trajectories re-enter the atmosphere or even pass through the earth's surface. To assure that this doesn't happen, the minimum altitude during the coast was computed (as part of the solution of the Lambert problem) and specified to lie outside the sensible atmosphere. The error between the computed minimum altitude and its specified value constituted, when set to zero, a third equality constraint.

Another way to implement the intercept condition is to integrate numerically the equations of motion of the final coast trajectory, just as the equations for the previous stages were integrated. In this case the errors between the inteceptor coordinates $r(t_f)$, $\theta(t_f)$ and the target coordinates at the

final time t_f are set equal to zero to form two equality constraints. As before, a minimum allowable altitude outside the sensible atmosphere can be chosen for the final coast trajectory. This minimum altitude is then the third constraint. Alternatively, the effect of the atmosphere itself, which is included in the trajectory equations, will ensure that a realistic altitude constraint is enforced when the final coast trajectory equations are integrated. Indeed, this is the required approach in the aero-assisted case, where the final coast trajectory actually utilizes aerodynamic down lift to hold the trajectory at near constant altitude in the presence of supercircular velocity. In Section 1.5 an example of this type is presented.

In addition to the equality constraints on the trajectory, inequality constraints may be imposed on some of the problem parameters. For example, an initial stage acceleration, $A_{\infty T}$, may have upper and lower limits, A_{\max} and A_{\min} . Direct treatment of these constraints in the algorithmic process was avoided by imposing them implicitly through the introduction a nonlinear transformation of a new parametric variable. In the case just mentioned a suitable transformation is

$$A_{\infty T}^0 = \frac{A_{\max} + A_{\min}}{2} + \frac{A_{\max} - A_{\min}}{2} \sin a_T \quad (1.12)$$

where a_T is the new unconstrained parameter.

Putting all of the above details together in a compact notation yields a problem of the form

$$\text{minimize } f(z) \text{ subject to } g_i(z) = 0, \quad i = 1, 2, 3. \quad (1.13)$$

Here: $f(z)$ is the ratio of the launch mass to the payload mass, the $g_i(z)$ are the errors in meeting the equality constraints, and z is a vector whose components are the "unconstrained" parameters arising from models described in Section 1.2. Given z , it is clear that $f(z)$ and $g_i(z)$ may be evaluated by integrating the equations of motion, computing $m(t_c)$, $\gamma(t_c)$, $V(t_c)$, $r(t_c)$, and $\theta(t_c)$, and solving the Lambert problem determined by the target specification. When the alternative method involving numerical integration of the final coast trajectory is used to implement the intercept condition, $f(z)$ was still evaluated from $m(t_c)$, but $g_i(z)$ is evaluated from $r(t_f)$ and $\theta(t_f)$.

The algorithm for the numerical solution of (1.13) requires the gradient (collection of N first partial derivatives) of functions such as $f(z)$. While it is possible to derive formulas for the partials (they may be written in terms of the differential equations adjoint to the linearized equations of motion), they are exceedingly complex because of the nonlinear functions appearing in Eqs. (1.1) - (1.9) and (1.11). This was the reason for using finite differences for the gradient calculations.

1.4 Numerical Solution of the Optimization Problem

A variety of numerical approaches have been used to solve trajectory optimization problems with equality constraints. These include: (1) gradient projection methods, (2) Newton-Raphson solution of the necessary conditions, (3) penalty function methods. Approach (1) gives slow convergence; approach (2) requires second derivatives of problem data and good initial estimates; approach (3) leads to badly conditioned (though unconstrained) minimization problems. In the research reported here approach (3) has been used, with its disadvantages attacked by using a rapidly convergent quasi-Newton algorithm [5,6] and an augmented Lagrangian for the penalty function.

In the usual penalty function method approximate solutions of (1.13) are sought by algorithmic minimization of

$$F_p(z) = f(z) + \sum_{i=1}^3 \mu_i [g_i(z)]^2 \quad (1.14)$$

It can be shown [5,6] that the equality conditions can be accurately enforced by choosing the penalty coefficients, $\mu_i > 0$, to be sufficiently large. In practice, numerical hazards, such as slow convergence or convergence to false minima, are reduced by minimizing $F_p(z)$ several times with successively larger values for the penalty coefficients. At each successive stage the starting point for the minimization algorithm is taken as the solution point from the previous stage. Even so, the conditioning of $F_p(z)$ worsens [5,6] as the μ_i increase and there is a practical limit to the accuracy which can be achieved. Numerical errors in the minimization algorithm and the evaluation of $F_p(z)$ and its gradient eventually become the limiting factors.

In the augmented Lagrangian approach $F_p(z)$ is replaced by

$$F_L(z) = f(z) + \sum_{i=1}^3 \lambda_i g_i(z) + \sum_{i=1}^3 \mu_i [g_i(z)]^2 \quad (1.15)$$

where the λ_i are real numbers approximating the Lagrange multipliers for the minimization problem (1.13). When $F_L(z)$ is minimized, it is possible to satisfy the equality constraints accurately with much smaller values for the penalty coefficients [5,6]. The resulting improved conditioning of $F_L(z)$ reduces the bad effects of the numerical errors. Again, it is advantageous to solve a sequence of minimization problems with successive initializations, where in this case both the λ_i

and the μ_i are adjusted. The adjustment scheme proposed by Powell and described on page 134 of [5] was used with good results in the research reported here. It eliminated the need for human intervention in selecting the parameters λ_i and μ_i and improved by at least an order of magnitude the accuracy of equality constraints over the simple penalty function approach.

Because of the highly nonlinear character of $F_L(z)$ and its poor conditioning, it was necessary to pay careful attention to the procedure for its unconstrained minimization. Certainly, the second order properties of $F_L(z)$ must be taken into account. The BFGS, quasi-Newton program of Shanno and Phua [7] was found to be effective. Its line search was modified to compute derivatives along the search direction directly by forward differences. This eliminated the need for gradient evaluations during the line search.

The performance of a quasi-Newton algorithm is predicated on the smoothness of the function being minimized. The function should be at least twice continuously differentiable. Here, the representation of empirical data appearing in the equations of motion is important. See, for example, the comments in Section 1.2 on computing the atmospheric density by table lookup with linear interpolation.

Another concern is the forward difference computation of the partial derivatives of $F_L(z)$. If the step size is too small, the effects of round off errors are exacerbated; if the step size is too large, truncation errors become appreciable. If the machine precision is ϵ , it can be argued [6] that the step size should be the order of $\epsilon^{1/2}$. In our case the machine precision $\epsilon @ 10^{-12}$ was determined by the AD 100, which has a 40 bit significand. It was found that the step size 10^{-6} was reasonable, but that experimentation with the step size could improve the accuracy noticeably. Even better accuracy was obtained by using central differences for the partial derivatives. It reduced the effects of round-off errors, since in this case a larger step size could be used for the same truncation error [6]. Of course, $2N + 1$ evaluations of $F_L(z)$ are then needed to obtain $F_L(z)$ and its gradient.

In general the trajectory state equations were solved numerically using fourth-order Runge-Kutta integration with a fixed step size. A single-pass predictor method with a Gear RK-4 startup algorithm was found to give better performance in some cases [8] and represents an area for further research.

1.5 Example Optimal Trajectory Solutions

Two example optimal trajectory solutions are considered in this section. $\theta(t_f) - \theta_0$, the total change in polar angle of each trajectory, is set equal to 30 degrees. This corresponds to an

interceptor range of 2094 miles. The total time of interceptor flight was prescribed to be 300 seconds and the target was intercepted at an altitude of 200 km. Stage takeoff weight was equal to 10,000 kg and physical parameters were assumed to be similar to those of a Minuteman III. The specific impulse I_{sp} of the rocket engines was equal to 300 seconds, and the ratio of initial fuel weight to inert weight for the rocket motor of each stage was assumed to be 10. The intercept condition was implemented by two equality constraints that required the interceptor coordinates at the final time t_f to match the target coordinates. Two cases were considered; aeroassisted and non-aeroassisted. In the aeroassisted case the final coasting stage reenters the earth's atmosphere with a controlled angle of attack which could generate downward lift. In the non-aeroassisted case the angle of attack of the final coasting stage was maintained at zero, which meant that aerodynamic forces could only cause drag. In each case there were 4 booster stages, with equal mass ratios prescribed for each stage. The common mass ratio was therefore a parameter. As noted earlier, the performance objective was to maximize the final payload weight. The results are summarized in Table 1.1.

TABLE 1.1. Optimal Trajectory Data for 4-stage Interceptor

	<u>Aeroassisted</u>	<u>Non-aeroassisted</u>
Final optimal payload weight	9.73 kg	5.63 kg
Mass ratio per stage	3.98	4.33
Minimum altitude in final coast to target	93.82 km	96.82 km
Burnout speed (V_C = circular orbit speed)	1.766 V_C	1.775 V_C
Burnout altitude	98.24 km	155.04 km
Launch flight path angle, γ_0	82.8 deg	60.6 deg
Initial thrust acceleration, stage 1	13.05 g	9.28 g
Burn time, stage 1	17.21 sec	24.86 sec
Coast time between stages 1 and 2	6.49 sec	1.84 sec
Initial thrust acceleration, stage 2	23.37 g	12.93 g
Burn time, stage 2	9.61 sec	17.84 sec
Coast time between stages 2 and 3	5.35 sec	2.41 sec
Initial thrust acceleration, stage 3	31.40 g	23.87 g
Burn time, stage 3	7.15 sec	9.67 sec
Coast time between stages 3 and 4	14.85 sec	56.74 sec
Initial thrust acceleration, stage 4	37.52 g	31.67 g
Burn time, stage 4	5.99 sec	7.29 sec
Final coast time to target	233.67 sec	179.36 sec
Total flight time	300 sec	300 sec
Total distance	2094 miles	2094 miles

From the table it is clear that the optimal aeroassisted trajectory yields a significantly larger payload, 9.73 kg versus 5.63 kg for the non-aeroassisted case. In Figure 1.1 are shown time

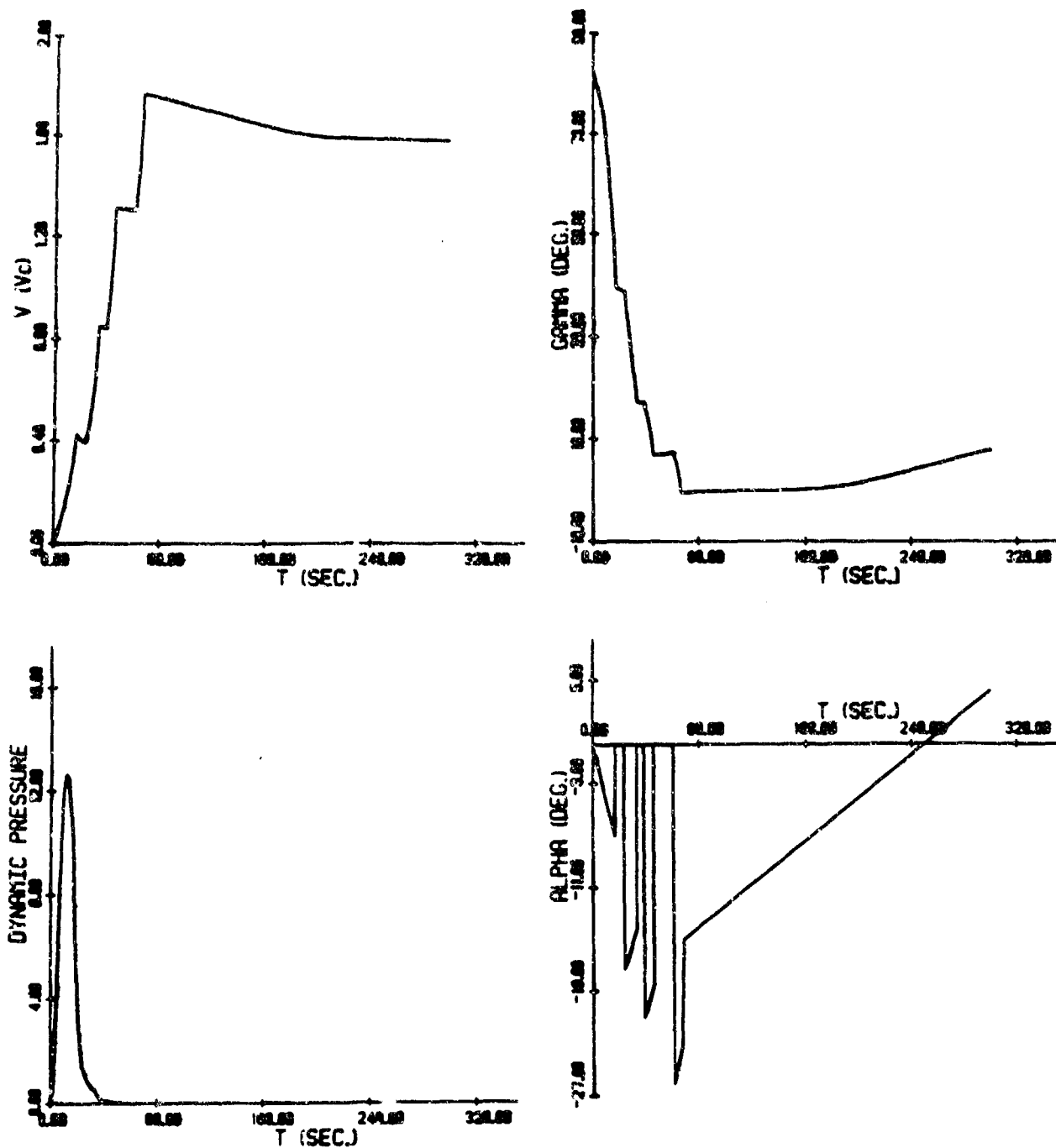


Figure 1.1. Time history plots for the aeroassisted optimal trajectory.

history plots of velocity, flight path angle, dynamic pressure and angle of attack for the aeroassisted optimal trajectory. Figure 1.2 shows altitude versus polar angle plots for both the aeroassisted and non-aeroassisted trajectories. Note how the aeroassisted trajectory is able to maintain an approximately constant altitude of some 95 km over more than half of the final coast to intercept. This is possible despite the supercircular speed because of the aerodynamic down lift, which reaches a maximum of 1.87 g during this portion of the trajectory. The maximum total downward acceleration, including gravity, is therefore 2.87g. Since the centrifugal acceleration in g units is V^2/r (where V is the circular-orbit velocity), it follows that constant altitude (i.e., a circular orbit) will, in the presence of 1.87 g of down lift, be maintained at a velocity of $(2.87)^{1/2}$ or $1.694V_c$. Reference to the plot of V versus time in Figure 1.1 shows that this is indeed the case. On the other hand we see in Figure 1.2 that the non-aeroassisted trajectory must climb to over 150 km before the final stage burn in order to avoid significant penetration of the atmosphere. This results in a considerably more expensive trajectory in terms of required mass ratio.

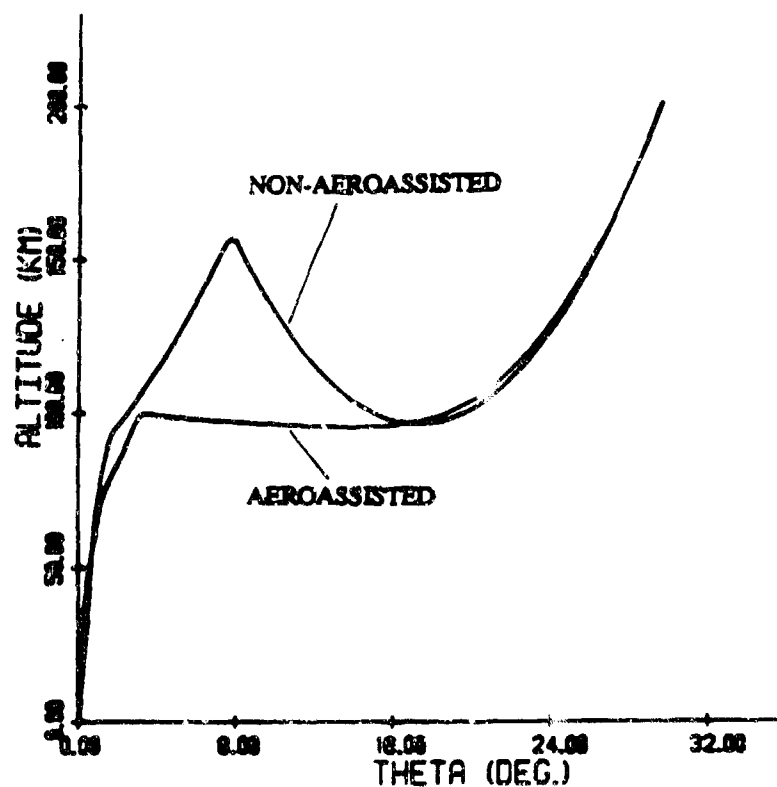


Figure 1.2 Comparison of optimal trajectories with and without aeroassistance.

The plot of angle of attack α versus time in Figure 1.1 shows clearly the linear variation of α for each stage. Note that zero angle of attack was assumed during the coast between stage burns. This was based on the assumption that the interceptor is aerodynamically stable during these coasts with no active thrust vector control. Means of active attitude control would be required to maintain the linear angle of attack variation shown for the final coast to intercept. One option for achieving this would be to provide thrust vector control utilizing a low level of thrust during this final portion of the trajectory. Such thrust will probably be required in any event to provide course corrections to intercept the target. When this is included in the overall trajectory optimization, it may very well produce a non-aeroassisted optimal trajectory which is competitive with the aeroassisted case, since now a downward component of thrust can be used to replace the aerodynamic down lift. It should be noted that boundary layer injection at hypersonic speeds, which is the subject of Part 2 of the research reported here, is also a candidate for attitude control while the interceptor is either coasting or thrusting in the atmosphere.

1.6 Optimal Intercept from a Space Base

The final stage of the computed trajectory is essentially a small rocket interceptor launched from space, i.e., from the ascending (n-1)th stage. Therefore, an analytic study of the optimal intercept trajectory has been made for the case of space launch from an orbiting platform. The launch base is assumed to be on a Keplerian orbit. The trajectory of the target is arbitrary, but it is assumed to be well determined after a time t_0 called the acquisition time. Again, the intercept time $t_f - t_0$ is restricted to several minutes.

For flight in a vacuum and in a central Newtonian force field with impulsive thrust, a complete analytical solution has been obtained. The study used the well established theory of the primer vector in optimal transfer. For a specified intercept time t_f , the one-impulse solution initiated at the time t_0 is assumed. The associated Lambert problem is solved and the magnitude of the required impulse is computed. The resulting initial conditions and the transversality conditions for optimality are sufficient to compute the primer vector which governs the optimal thrust control. Then, based on the information provided by the primer vector, rules have been established to search for the optimal solution if the assumed initial one-impulse trajectory is not optimal. It has been found that there are three possible optimal trajectories.

- a. One impulse trajectory with the thrust applied immediately at the acquisition time t_0 .
- b. One-impulse with an initial coasting phase until the optimal time $t_1 > t_0$ before the application of the impulse.

c. Two-impulse trajectory with the first impulse at t_0 and the second impulse at mid-course for final interception.

The theory can be used to explain the necessary coast time between the n th stage of the previously computed optimal trajectories for a multi-stage interceptor launched from the surface of the earth.

A numerical example has been used to test the theory. The interceptor is launched from a base in a circular orbit at 600 km altitude. The target is intercepted at an altitude of 250 km with a down range longitude of 45 degrees and various latitudes ranging from 0 to 60 degrees. The intercept times range from 2 minutes to 15 minutes. For each case the maximum characteristic velocity for intercept is computed. Depending on the prescribed intercept time, the trajectory may change from an elliptic trajectory to a clearly hyperbolic trajectory.

1.7 Guidance and Control to Intercept of the Final Stage

To provide terminal control out of the atmosphere so the final stage can home on the target requires some type of guidance law and trajectory control. The trajectory can be changed by providing acceleration at right angles to the interceptor flight path. For an interceptor which utilizes a fixed rocket engine to provide acceleration along its longitudinal axis, a required lateral acceleration component can be generated by the appropriate change in attitude angle.

To minimize weight and complexity, an attitude control method which uses only a single small control jet has been studied. This single jet provides thrust at right angles to the longitudinal axis of an axially-symmetric terminal stage. The stage is given a large roll rate about its longitudinal axis, along which the main rocket engine provides continuous thrust. Attitude control is achieved by turning on the small side jet for a fraction of each revolution and at the right time during the roll cycle. A simple incremental change in attitude of the spinning stage can be viewed as a change in direction of its angular momentum vector without a change in vector magnitude. Each discrete change in attitude requires at least two impulses from the control jet. The first impulse produces an increment in angular momentum at right angles to the spin axis. The second control jet impulse is applied half a roll period later to cancel the angular momentum increment at right angles to the spin axis, which has now been changed in direction by the attitude angle increment. The size of the incremental change in attitude angle can be varied by changing the thrust duration of the control jet. If the available thrust is insufficient to change the attitude by the desired amount, then a number of cyclic impulses followed by the same number of cyclic impulses initiated half a period later can be utilized.

The dynamics of the above control scheme has been studied using both analytic methods and computer simulation. Minimum resolution in attitude angle has been established as a function of system parameters, including minimum control-jet thrusting time. Multiple thrust maneuvers for large attitude changes have also been studied in the same manner. Required control laws for achieving desired attitude angle changes have been developed.

Once a means of attitude control is available, a guidance law is needed to specify the required trajectory changes. The most commonly used guidance law for homing missiles is proportional navigation. Here it does not appear to be a practical guidance method because it results in excessive terminal accelerations for the interceptor. As an alternative, a simple algorithm has been developed to estimate the future positions of both interceptor and target. Based on target position, velocity and acceleration, and the known equations of motion, a power series solution for future target position is obtained. In the same way, the future interceptor position is computed. From these predicted trajectories the required interceptor attitude for zero miss is calculated and utilized to implement the guidance law. Computer simulations have been used to test the effectiveness of this method in combination with the single-axis attitude control scheme described above. The simulations have been run for both thrusting and coasting targets. Based on reasonable interceptor parameters, including roll rates, control-thrust levels, and minimum control-thrust times it has been determined that direct hits can be obtained. However, these simulations have not yet taken into account the effect of guidance measurement errors, nor have they considered the effect of target thrust termination during terminal guidance of the interceptor.

1.8 Conclusions and Subsequent Research

This research has considered techniques for computing the optimal trajectories of earth-launched interceptor rockets which are accelerated to over twice orbital velocity. The objective of the optimization is to maximize the payload with a given interceptor takeoff weight. Terminal constraints have been enforced using penalty functions. The required gradients of the cost functions have been computed numerically using finite differences. Results have been presented for a 4-stage example. It was found that allowing a coast period between booster stages and using an aeroassisted trajectory to generate down lift during the final coast segment improves the optimal payload significantly. The research has also considered attitude control of a final interceptor stage which uses a fixed rocket engine to provide thrust along its longitudinal axis, about which the rocket also spins. Attitude changes are achieved by firing a single small thruster at right angles to the spin axis at the appropriate time during each spin cycle. In combination with a guidance law based on predicted future target and interceptor trajectories, it has been found through computer simulation that direct hits can be obtained.

Future optimal trajectory research efforts will include parametric studies of the effect of different prescribed flight times, target range and altitude, payload mass, and refined aerodynamic and propulsion models. The effect of aerodynamic heating on the ascent trajectory and during the aeroassisted terminal trajectory will also be studied. Optimal trajectories for the case where the final coast to the target is replaced by a thrusting stage will also be determined. The problem of optimal intercept from a space base will be extended to the case where the carrier is an ascending rocket, namely, the (n-1)th stage, and to the case where the carrier is a supersonic aircraft maneuvering at high altitude.

Additional research on methods of guidance and control of the final interceptor stage will consider the use of more accurate target and interceptor prediction methods, the effect of guidance measurement errors, and the effect of uncertainty in target thrust termination time. The influence of each of these effects on the performance attainable with the single-jet attitude control scheme will be studied.

1.9 References

- [1] N.X. Vinh, A. Buseman and R.D. Culp, *Hypersonic and Planetary Entry Flight Mechanics*, The University of Michigan Press, Ann Arbor, Michigan, 1980.
- [2] L.H. Jorgensen, "Estimation of Aerodynamics for Slender Bodies Alone and with Lifting Surfaces," *AIAA Journal*, Vol. 11, No. 3.
- [3] *U.S. Standard Atmosphere Supplements*, 1966, U.S. Government Printing Office, Washington D.C.
- [4] R. H. Battin, "An Elegant Lambert Algorithm," *Journ. Guidance, Control, and Dynamics*, vol. 7, pp. 662-670, 1984.
- [5] R. Fletcher, *Practical Methods of Optimization*, vol. 2, Wiley-Interscience, 1981.
- [6] P. E. Gill, W. Murray and M. H. Wright, *Practical Optimization*, Academic Press, 1981.
- [7] D. F. Shanno and K.H. Phua, "Minimization of Unconstrained Multivariate Functions," *ACM Transactions on Mathematical Software*, vol. 6, pp. 618-622, 1980.
- [8] R.M. Howe, E.G. Gilbert, Ping Lu, G. Shorr, N.X. Vinh, "Computation of Optimal Trajectories Using State-of-the-art Simulation Technology," to appear in *Proceedings of the Conference on Aerospace Simulation*, no. 3, Feb. 3-5, 1988, San Diego, California.

2. Investigation of the Control of Aerodynamic Forces on Hypersonic Vehicles by Boundary Layer Injection

Thomas C. Adamson, Jr., Principal Investigator

Arthur F. Messiter, Co-Investigator

Bram van Leer, Co-Investigator

Nelson Carter, Graduate Student

Michael Matarrese, Graduate Student

A great deal of work on hypersonic flow was done in the period 1955-1970, with some attention paid to boundary layer blowing. Although the greatest part of this work had to do with the flow over blunt bodies, there were some studies involving slender bodies. More importantly, multi-component flows, dissociation of the air, gas reactions involving effluents from the surface, and the strong effects of heat transfer received much attention in those analyses. Because numerical techniques were in their infancy, analytical methods and the necessary attendant simplifying assumptions were used. In the meantime, the use of computational methods has come to the forefront and more realistic closure models have allowed the numerical analysis of turbulent boundary layers. Nevertheless, the literature has much to offer for this problem and so the first few months of this effort were used in a literature search. Particular emphasis was given to papers on gas injection into boundary layers in hypersonic flows, or at least compressible flows, on hypersonic flow over slender bodies, and particularly over wedges, and on multi-component flow fields, and in particular, the calculation of multi-component transport properties.

The problem considered is that of two-dimensional hypersonic flow over a slender wedge, from the upper surface of which a gas, not necessarily air, is blown. Figure 2.1 contains sketches of the case where the blowing is distributed over the whole surface (2.1a) and the case where it is confined to strips (2.1b), and illustrates the notation employed. It should be noted that $s(x)$ is indicated to be the distribution of effective body shape. Since it is measured relative to the surface of the wedge, it is a displacement thickness. For strong blowing, that is when the viscous boundary layer is blown off the wall, and moreover, for the case where this viscous layer is thin compared to the blown layer thickness, the displacement thickness corresponds to the separating streamline; i.e., all the blown gas flow lies within some bounding streamline. For other conditions, when the viscous layer is not thin, a displacement thickness must be calculated. In Figure 2.1b, the shapes $s_1(x)$, $s_2(x)$,... indicate the displacement thickness distributions for the flow resulting from all the strips except the first ($s_1(x)$), all except the first two ($s_2(x)$) etc. Just as in typical boundary layer theory, one can consider the thickness of a concentration layer consisting of the region into which the injected gas is blown and/or diffuses. For example, following usual

practice, the edge of the layer might be defined as the line along which the concentration of injected gas is a very small constant; of course this line is not a streamline. The order of magnitude of the ratio of the thickness of this layer to the displacement thickness depends on the case under consideration. Thus, for the case where the injection velocity is of the same order as the v velocity component in the boundary layer and the injected gas mixes with the boundary layer air (weak blowing), the order of this ratio depends upon the Schmidt number. Indeed, the effect upon this ratio of the ratio of the molecular weight of the blown gas to the molecular weight of air may prove to be an important parameter in the problem of obtaining a given pressure distribution for a minimum amount of blown gas. In any event, the fundamental problem considered is that of ascertaining the effective body shape $s(x)$ for a given blowing distribution $v_w(x)$ so that the corresponding pressure distribution on the wall or body surface can be calculated; finally it is desired to solve the inverse problem so that the blowing distribution $v_w(x)$ can be found for a desired pressure distribution $p_w(x)$.

In hypersonic flow without blowing, the shock wave on a slender wedge lies close to the body and thus to the boundary layer over the body. For some conditions, the inviscid shock layer downstream of the shock wave has a thickness large compared to the boundary layer thickness and for others may be of the same order of magnitude, and in fact, may merge with the boundary layer. In addition, if the nose is slightly rounded, the shock wave is detached and a thin high entropy layer is found adjoining the wall. The parameters which control the type of flow field found are the Mach number of the free stream M_∞ , the Reynolds number based on the free stream properties and the body length Re_∞ , and the wedge angle θ and nose radius. The hypersonic similarity parameter, written as $M_\infty \theta$ in terms of the parameters already defined, is taken to be $O(1)$ or large compared to one for hypersonic flow. The parameter which characterizes the relative order of the thicknesses mentioned above is the viscous interaction parameter

$$\chi_L = \frac{c M_\infty^3}{\sqrt{Re_{L_\infty}}} \quad (2.1)$$

where c is a constant. Thus for $\chi_L \ll 1$, there is a weak interaction between the inviscid and boundary layer flow; in other words, the boundary layer is thin compared to the shock layer. As χ_L increases, the boundary layer becomes thicker relative to the shock layer until a strong interaction occurs; then, they are the same order of magnitude and the solutions for each layer must be found simultaneously. Finally, for

$$\chi_L = 0 (M_\infty^2) \quad (2.2)$$

and for $\chi_L \gg M_\infty^2$, the layers are merged; they are indistinguishable.

When gas injection is introduced, as an additional mechanism to change the displacement thickness, it is still instructive to characterize the flow using χ_L . However, now the ratio of the order of the displacement thickness without blowing to that with blowing δ^*/δ_b^* may be used in addition, as indicated in Figure 2.2, where various physical problems and flow structures are associated with parametric regimes. It should be noted that there are no definite limits on any of the regimes. The dashed lines are drawn arbitrarily simply to illustrate that there are different regions in the sketch; in actuality, there is a gradual change from one flow regime to the next. It is instructive to picture the flow fields associated with various parametric regimes shown in Figure 2.2. Several such pictures for a flow over a half wedge are shown in Figure 2.3, where the identifying letters correspond to those in the circles in the sketch in Figure 2.2. For both weak and strong blowing, as χ_L increases, merged layers (not shown in Figure 2.3) occur. As seen in Figure 2.3, the most striking feature of the flow field with blowing is that as the blowing velocity increases, the boundary layer can be completely blown off the wall. It is this feature which will be used to characterize the terms weak and strong blowing. Thus, as long as the boundary layer is attached, the blowing is weak, while for strong blowing the boundary layer is blown off the wall.

It was decided to attack the problem from two different viewpoints. First, one of the important problems in developing a computational method of solution for compressible flow is the location and crispness of the shock wave. This is a more difficult problem in hypersonic flow over a slender body because the shock wave is at a relatively small angle relative to the direction of the undisturbed flow. Hence, work is being done on developing a code which will handle flow over slender bodies with arbitrary shape, corresponding to a wedge with blowing. Since the inviscid flow over an effective body (physical body plus displacement thickness) is being considered, the Euler equations are being solved. The other point of view under consideration has to do with the analyses of the near wall layers when blowing takes place. It was decided to consider the hard blowing case first for two reasons. First, the weak blowing case is essentially contained in the hard blowing formulation; i.e. no new mechanisms need be considered. Second, one of the

important sub-cases in the hard blowing formulation is that where the viscous shear layer, which results when the boundary layer is blown off the wall, is thin compared to both the blown layer and the shock layer. Hence the problems is as sketched in case (c) in Figure 2.3, and it is seen that for distributed blowing over the whole surface, the flow is inviscid. Thus, solutions found analytically could also be calculated numerically, because in this special case the whole flow field is inviscid; such test problems can be used to validate the numerical code as well as give useful information. Moreover, the extension to the case where the viscous shear layer thickness is no longer negligible is relatively simple. The work discussed in this report, then, is concerned with numerical solutions to the inviscid flow equations (Euler equations) and to solutions relating the equivalent body shape to the distribution of blowing velocity at the wall for the case of strong blowing; in the latter case problems with flow fields similar to those shown in both (c) and (d) of Figure 2.3 are considered.

2.1 Analytical Approach

In the analyses which follow, the lengths are made dimensionless with respect to a length L (overbars denote dimensional quantities) which for the present is arbitrary, but which will be used later to denote the length of the body. Moreover, the dimension normal to the flow is ordered by δ_L^* , the basic small parameter of the problem, and defined as the value of the nondimensional displacement thickness at $x = 1$ ($\bar{x} = L$). Thus \tilde{y} and the displacement thickness are denoted by

$$\tilde{y} = y/\delta_L^* \quad (2.3a)$$

$$y_d = \delta_L^* s(x) \quad (2.3b)$$

where, as previously indicated, $s(x)$ gives the distribution of displacement thickness. For $\chi_L \ll 1$, y_d is the dividing streamline between the blown flow and the shock layer flow; the viscous shear layer of negligible thickness lies along y_d also.

If \bar{P}_∞ , $\bar{\rho}_\infty$, and \bar{U}_∞ are the undisturbed pressure, density, and velocity respectively, then asymptotic expansions for the velocity components and the pressure are, for the case where blowing is small enough that the blown layer flow is incompressible,

$$\bar{q}_x = \bar{U}_\infty (\delta_L^*)^{1/2} u(x, \tilde{y}) + \dots \quad (2.4a)$$

$$\bar{q}_y = \bar{U}_\infty (\delta_L^*)^{3/2} v(x, \tilde{y}) + \dots \quad (2.4b)$$

$$\bar{p} - \bar{p}_\infty = \bar{\rho}_\infty \bar{U}_\infty^2 \delta_L^* \tilde{p}(x, \tilde{y}) + \dots \quad (2.4c)$$

Here \bar{q}_x and \bar{q}_y are the velocity components in the x and y directions respectively. If the blowing velocity is large enough that the blown layer flow is compressible then,

$$\bar{q}_x = \left(\frac{R_o \bar{T}_w}{\bar{m}_w} \right)^{1/2} u(x, \tilde{y}) + \dots \quad (2.5a)$$

$$\bar{q}_y = \left(\frac{R_o \bar{T}_w}{\bar{m}_w} \right)^{1/2} \delta_L^* v(x, \tilde{y}) + \dots \quad (2.5b)$$

$$\bar{p} = \bar{\rho}_\infty \bar{U}_\infty^2 (\delta_L^*) \tilde{p}(x, \tilde{y}) + \dots \quad (2.5c)$$

where $\bar{p}_\infty \ll \bar{p}$ and is neglected, R_o is the universal gas constant and \bar{T}_w and \bar{m}_w are the gas temperature at the wall and the molecular weight of the gas injected at the wall, respectively.

At hypersonic speeds the boundary layer along a solid surface can have a significant displacement effect on the external inviscid flow, an effect which can be greatly increased by surface blowing. Blowing at any flight speed can be strong enough that the boundary layer leaves the surface and the thickness of the "blown layer" is large in comparison with that of the separated free shear layer. This "blowhard" problem has been studied for several cases by Cole and Aroesty [1], using a systematic asymptotic approach. Their work has been chosen as the starting point for the analytical part of the present study.

Cole and Aroesty consider thin shapes and show that the pressure in the blown layer depends, in a first approximation, only on the streamwise coordinate x. In most of their examples,

the results express the shape of the dividing streamline, which separates the blown gas from the air which has passed through the shock wave from the leading edge, in terms of the blowing velocity and the pressure distribution.

To obtain a general idea of the magnitudes of the aerodynamic forces available through blowing, the first rather simple calculation concerned hypersonic flow past a wedge, with a thin ogival shape chosen for the dividing streamline; i.e. for this calculation, $s(x)$ was chosen, and the required $v_w(x)$ and the resulting $\tilde{p}(x)$ were calculated.. For a blown-layer thickness small in comparison with the wedge thickness, the small pressure perturbation is linear in the slope of the dividing streamline, and for constant surface temperature the density is nearly constant in the blown layer. The streamwise velocity component in the blown layer is then found in terms of the pressure from the incompressible form of the Bernoulli equation. Integration of the definition of the stream function leads to an expression for the scaled dividing-streamline shape $s(x)$ in terms of the surface blowing velocity $v_w(x)$ and the pressure $\tilde{p}(x)$:

$$s(x) = \left(\frac{\bar{p}_w}{2\bar{p}_\infty} \right)^{1/2} \int_0^x \frac{v_w(\xi) d\xi}{\{\tilde{p}(\xi) - \tilde{p}(x)\}^{1/2}} \quad (2.6)$$

Inversion of the integral equation and substitution of the linearized pressure formula for supersonic flow provides an explicit expression for v_w in terms of \tilde{p} .

For an ogival $s(x)$ it is easy to evaluate the resulting integral analytically. The results can then be converted to a plot of mass flow against force, as shown in Figure 2.4 for particular values of the parameters. If there were no blowing, the pressure force on the wedge surface (normalized in the same way as in the figure) would be, in the appropriate limiting case, $\{(\gamma+1)\theta^2/2\} \times 10^3 \cong 23$. The values shown in the figure are as large as one-half this value.

If the blowing velocity is somewhat larger, the blown-layer thickness is no longer small in comparison with the wedge thickness. The relative pressure change caused by the blowing also is no longer small, and density changes in the blown layer can not be neglected, so that the compressible Bernoulli equation is required. The scaled dividing-streamline shape is now

$$s(x) = \left(\frac{\gamma-1}{2\gamma}\right)^{1/2} \int_0^x v_w(\xi) \left\{ \frac{\tilde{p}(\xi)}{\tilde{p}(x)} \right\}^{1/\gamma} \left\{ H_0(\xi) \left[1 - \frac{\tilde{p}(x)}{\tilde{p}(\xi)} \right]^{(\gamma-1)/\gamma} \right\}^{-1/2} d\xi \quad (2.7)$$

where H_0 = total enthalpy. A curve similar to that in Figure 2.4 is obtained by numerical integration, and shows (Figure 2.4) the increased force available with these larger mass-flow rates.

Additional curves for the latter case of a compressible blown layer are shown in Figure 2.5 for a dividing streamline $s(x) = (\text{const.}) \{1 - (1-x)^3\}$, $0 < x < 1$, and $s'(x) = 0$, $x > 1$. That is, the dividing streamline becomes parallel to the wedge surface at $x = 1$, with continuous curvature. It is found that the blowing velocity then approaches zero at $x = 1$, as seen in the figure. If instead, as in Figure 2.6, $s(x) = (\text{const.}) \{1 - (1-x)^2\}$, $0 < x < 1$, and $s'(x) = 0$, $x > 1$, the blowing velocity drops to zero discontinuously. These results are consistent with series expansions of the integral equation about $x = 1$ which have been carried out for the two cases. These cases are helpful not only in illustrating levels of available forces, but also in indicating the constraints on v_w when blowing is stopped at some point, as in strip blowing.

By contrast, the pressure forces for very weak blowing may be too small to be useful. For a laminar boundary layer, the displacement thickness for high Mach number is $\delta^* \approx 0.1 M_\infty^2 x / \sqrt{Re_x}$, where Re_x is the Reynolds number based on free-stream quantities and x , and a linear viscosity-temperature law has been assumed for simplicity. Without blowing, the resulting pressure perturbation is linear in the slope of the equivalent displacement surface, giving a pressure force (again normalized as in Figure 2.4) of about 0.3 for $Re_x = 10^5$ and for the wedge angle and Mach number of Figure 2.4. With blowing this would be multiplied by a numerical factor, say 2 or 3, and clearly is still far smaller than typical values in Figure 2.4.

As mentioned above, some effort has been spent on ascertaining the various sets of conditions which can or must exist as $v_w(x) \rightarrow 0$ at a given point on the wedge surface. Such analysis is necessary in order to handle properly the solutions for strip blowing and indeed blowing with multiple strips. It is evident from physical considerations and illustrated in Figures 2.5 and 2.6 that over the length of the wedge the wall pressure must decrease if the gas in the blown layer is to go downstream. That is, the pressure gradient in the y direction is negligible and so the pressure distribution at the wall is that which holds throughout the blown layer; if the pressure rose, the fluid would be accelerated upstream. However, it may be desirable to obtain

pressure distributions quite different from those shown in Figures 2.5 and 2.6, so various distributions of $v_w(x)$ must be considered. Strip blowing is a variation with promise because it appears to allow for local increases in pressure. That is, from Figure 2.1b, with supersonic flow over $s(x)$, it is seen that at each discontinuity in $s(x)$ the pressure would rise in a short distance, then decrease again as x increases. The result appears to be several local increases in $\tilde{p}(x)$ each followed by a decrease; with the average pressure decreasing as one goes from the vertex of the wedge to some downstream point. This will allow for a quite different \tilde{p} distribution from those found from the $s(x)$ and $v_w(x)$ distributions given in Figures 2.5 and 2.6.

At the end of a strip, the manner in which $v_w(x) \rightarrow 0$ affects the distribution of $s(x)$ and thus of $\tilde{p}(x)$. It can be shown that $s'(x) = 0$ there if there are no other mechanisms to change the pressure. From Equation 2.7, then, this can be shown to require that $v_w(x) \rightarrow 0$ continuously rather than discontinuously. The manner in which $v_w \rightarrow 0$ for a given flow field, i.e. the functional form needed to assure that $s'(x) \rightarrow 0$ continuously is found using the derivative of Equation 2.7, which relates $s'(x)$ to $v_w(x)$ and $\tilde{p}(x)$, and another equation relating two of the three unknowns. For first calculations, the tangent wedge approximation is being used. The resulting equation for $\tilde{p}(x)$ and the equation showing the proper order of θ_w are:

$$\tilde{p}(x) = \left(\frac{\gamma + 1}{2} \right) (s'(x) + \bar{\theta}_w)^2 \quad (2.8a)$$

$$\theta_w = (\delta_L^*) \bar{\theta}_w \quad (2.8b)$$

The final relation with which one works is an integro-differential equation, of complex form. The analysis leading to the functional form for $v_w(x)$, and thus for $s(x)$ and $\tilde{p}(x)$, which is physically correct and gives non-singular behavior at the edge of the strip, as well as the form of the solution at the beginning of the next strip, is presently being carried out.

The flows considered so far are for $\chi_L \ll 1$; i.e. the flow pictures resemble that in sketch (c) in Figure 2.3. As χ_L increases, the shear layer is no longer of negligible thickness, but of the order of the blown layer and shock layer thicknesses; i.e., all are the same order and a strong interaction takes place. Then the flow appears as shown in sketch (d) of Figure 2.3 and in more detail at the top of Figure 2.7. This case also occurs for the flow shown in sketch (c) of Figure 2.3 as the vertex or leading edge of the wedge is approached; i.e. the flow first follows sketch (d) for $x \ll 1$, and then follows sketch (c) for $x = O(1)$. In the following, the case where the shear layer thickness is no longer of negligible thickness compared to the other layers is considered for hypersonic flow over a flat plate, for simplicity.

For a flat plate, then, again using a linear viscosity-temperature law, the boundary-layer thickness $O(M_\infty^2/\sqrt{Re_x})$ is small in comparison with the shock-layer thickness $O(1/M_\infty)$ when $x \gg M_\infty^6 \bar{\nu}_\infty/\bar{U}_\infty$, where $\bar{\nu}_\infty/\bar{U}_\infty$ is a viscous length based on free-stream quantities; $\bar{\nu}_\infty$ is the kinematic viscosity in the undisturbed flow. In this range the interaction of the boundary-layer with the external flow is a "weak" interaction, since the boundary-layer flow can be calculated first and the correction to the external flow determined later. For $x = O(M_\infty^6 \bar{\nu}_\infty/\bar{U}_\infty)$ the boundary layer and external flow must be calculated simultaneously, because the boundary-layer and shock-layer thickness are of the same order of magnitude in M_∞ and Re_x . In the range $M_\infty^2 \bar{\nu}_\infty/\bar{U}_\infty \ll x \ll M_\infty^6 \bar{\nu}_\infty/\bar{U}_\infty$ the interaction is called a "strong" interaction, and coupled self-similar solutions are available for the boundary layer and shock layer. When $x = O(M_\infty^2 \bar{\nu}_\infty/\bar{U}_\infty)$ ("merged-layer regime"), length scales in both directions are of the same order, and the different flow regions are no longer distinct.

As indicated above, for strong blowing it is anticipated that there may be a significant flow region where the shear-layer thickness can not be neglected. To gain some understanding of the accompanying force changes, and for later comparison with numerical calculations, the case of strong interaction with strong blowing is being studied. The blown layer, shear layer, and shock layer are distinct, with self-similar solutions available in each region. These can be obtained separately, with a coupling arising primarily because the location of one layer depends on the displacement thickness of the layer(s) below it.

To illustrate the nature of the solution, the form of the transverse velocity component v in each of the three regions is as shown below, in terms of the appropriate similarity variables. The stream function $\bar{\psi}$ is defined in the usual way by $\partial\bar{\psi}/\partial\bar{y} = \bar{\rho} \bar{q}_x$; the coordinate \bar{x} is defined by $\bar{x} = (\bar{U}_\infty \bar{x}/\bar{\nu}_\infty)/M_\infty^6$, so that the strong-interaction range is $M_\infty^{-4} \ll \bar{x} \ll 1$.

$$\text{blown layer: } v = \left(\frac{\bar{U}_\infty \bar{x}}{\bar{\nu}_\infty M_\infty^6} \right)^{-1/2} \bar{v}_1(\bar{\xi}), \quad \bar{\xi} = M_\infty \left(\frac{\bar{\psi}}{\bar{\rho}_\infty \bar{\nu}_\infty M_\infty^6} \right) / \left(\frac{\bar{U}_\infty \bar{x}}{\bar{\nu}_\infty M_\infty^6} \right)^{1/2} \quad (2.9a,b)$$

$$\text{shear layer: } v = \left(\frac{\bar{U}_\infty \bar{x}}{\bar{\nu}_\infty M_\infty^6} \right)^{-1/4} \bar{v}_1(\bar{\xi}), \quad \bar{\xi} = M_\infty^2 \left(\frac{\bar{\psi}}{\bar{\rho}_\infty \bar{\nu}_\infty M_\infty^6} \right) / \left(\frac{\bar{U}_\infty \bar{x}}{\bar{\nu}_\infty M_\infty^6} \right)^{1/4} \quad (2.9c,d)$$

$$\text{shock layer: } v = \left(\frac{\bar{U}_\infty \bar{x}}{\bar{\nu}_\infty M_\infty^6} \right)^{-1/4} \bar{v}_1(\bar{\xi}), \quad \bar{\xi} = \left(\frac{\bar{\psi}}{\bar{\rho}_\infty \bar{\nu}_\infty M_\infty^6} \right) / \left(\frac{\bar{U}_\infty \bar{x}}{\bar{\nu}_\infty M_\infty^6} \right)^{3/4} \quad (2.9e,f)$$

The solution for the blown layer is found from the results of Cole and Aroesty [1]. In particular, the surface blowing velocity $\bar{v}_w = (\text{const.}) \bar{U}_\infty / \sqrt{x}$ is found to give surface pressures $\bar{p} = (\text{const.}) \bar{\rho}_\infty \bar{U}_\infty^2 / \sqrt{x}$, consistent with the conventional strong-interaction theory but with a larger constant factor, which is to be determined. The solution for the shear layer is found by numerical integration of the compressible boundary-layer equations in self-similar form; velocity and total-enthalpy profiles are shown in Figure 2.7. The solution for the inviscid shock layer requires numerical integration of the self-similar hypersonic small-disturbance equations, which is currently being carried out.

2.2 Numerical Approach

The computation of hypersonic flows, in the Mach-number range 8-30, puts before the computational fluid dynamicist a number of problems not encountered in the lower Mach-number range. One problem is the loss of accuracy of conventional finite-volume methods when "capturing" strongly oblique discontinuities; more problems are encountered in marching to a steady state, where loss of positivity of certain state quantities, non-uniqueness of discrete solutions (recently found at NASA Langley Research Center) and general inefficiency of classical relaxation methods on vector computers all contribute to slowing down or even halting the convergence process. Many of these problems have to be addressed when computing the two-dimensional hypersonic flow over a wedge with surface blowing, which is the theme of the present work.

In the period covered by this report, emphasis was put on the question of accuracy, although matters of computational economy are not ignored, as will become evident below.

The representation of discontinuities oblique to the computational grid with high resolution is a fundamental problem which at present is being considered only by a handful of researchers. It would be easier to ignore it and simply rely on the capacities of today's supercomputers, namely, by using greatly refined grids. Such a strategy has often forestalled advances in computational algorithms, especially in research environments equipped with the latest, top-of-the-line computers, and eventually backfires. In the present situation it is the pursuit of three-dimensional flow simulations that necessitates the development of high-resolution algorithms, since the number of nodal points per dimension drops significantly.

There are two ways to improve the resolution of a flow computation without unduly taxing the CPU budget; local grid refinement, and local reconstruction of discontinuities. These are independent techniques that may complement each other in practice, and both are equally worthy of research effort and support. Here, it has been decided to develop the latter technique, although funding has been requested from other sources for developing grid-adaptation techniques, in parallel to this work.

A study of the literature on the subject of "jump recovery" at the start of the period, and discussions of the subject with a few active in the field (S. F. Davis, NSWC, P. L. Roe, Cranfield, and C. Hirsch, Brussels) during the summer have led to the following insights:

- (a) there are several models of local flow that can provide information about strong waves present in a discrete (finite-volume) solution;
- (b) no one knows exactly how to include this information in a computational flow algorithm that is stable and yields the desired accuracy.

While apparently the greatest challenge is in (b), there is still ample room for ideas regarding the modelling of local flow based on limited discrete data.

Following an approach previously indicated in Reference [2], the initial work was begun with a least-squares analysis of the local flow field based on only two sets of flow quantities, describing the averaged states in two adjacent cells of fluid. If these states can be connected by a single oblique discontinuity, they should satisfy the jump equations

$$V[Q] = [f] \cos \alpha + [g] \sin \alpha, \quad (2.10)$$

where Q is the state vector (components: mass, momentum and energy density), f and g are the flux vectors in a cartesian frame, α is the direct angle of the normal to the wave front, v is the wave velocity, and $[..]$ denotes a jump (see Figure 2.8). In computational practice, exact satisfaction of these equations never happens, but a set of values (α, V) may be sought that minimizes the length of the residual vector r :

$$r = -V[Q] + [f] \cos \alpha + [g] \sin \alpha \quad (2.11)$$

If the notation (\dots) is used for an inner product, then

$$\begin{aligned} (r,r) &= V^2([Q], [Q]) - 2V([Q], [f] \cos \alpha + [g] \sin \alpha) \\ &\quad + ([f] \cos \alpha + [g] \sin \alpha, [f] \cos \alpha + [g] \sin \alpha) \end{aligned} \quad (2.12)$$

which, for fixed α , reaches a minimum for

$$V = \{([Q], [f]) \cos \alpha + ([Q], [g]) \sin \alpha\} / ([Q], [Q]) \quad (2.13)$$

With this choice of V ,

$$\begin{aligned} r &= \left\{ [f] - \frac{([Q], [f])}{([Q], [Q])} [Q] \right\} \cos \alpha + \left\{ [g] - \frac{([Q], [g])}{([Q], [Q])} [Q] \right\} \sin \alpha \\ &\equiv a \cos \alpha + b \sin \alpha \end{aligned} \quad (2.14)$$

Therefore

$$\begin{aligned} \min_V (r,r) &= (a,a) \cos^2 \alpha + 2(a,b) \sin \alpha \cos \alpha + (b,b) \sin^2 \alpha \\ &= \frac{1}{2} \{ (a,a) - (b,b) \} \cos 2\alpha + (a,b) \sin 2\alpha + \frac{1}{2} \{ (a,a) + (b,b) \} \end{aligned} \quad (2.15)$$

Now ψ is defined such that

$$\tan 2\psi = 2(a,b) / \{ (a,a) - (b,b) \} \quad (2.16)$$

More specifically,

$$\sin 2\psi = -2(a,b)/h, \quad (2.17)$$

$$\cos 2\psi = -\{ (a,a) - (b,b) \} / h, \quad (2.18)$$

$$h = \sqrt{ \{ (a,a) - (b,b) \}^2 + 4(a,b)^2 } \quad (2.19)$$

Then

$$\min_V (r,r) = -\frac{h}{2} \cos 2(\alpha - \psi) + \frac{1}{2} \{ (a,a) + (b,b) \} \quad (2.20)$$

which reaches its minimum value for

$$\alpha = \psi + \kappa\pi \quad (2.21)$$

It is convenient to adopt

$$\alpha = \psi \quad (2.22)$$

as the essential solution; with $\alpha = \psi + \pi$ there is only a change of sign in V . To find V , (2.22) is inserted into (2.13).

There is one degenerate case, namely

$$[Q] // [f] // [g] \quad (2.23)$$

leading to $a = b = 0$. This occurs for the inviscid flow equations when the wave shows up only as a density (or entropy) fluctuation. Such a wave is linear, implying that the wave's velocity vector is independent of the fluctuations it causes. In this case the normal to the wave front is not meaningful; the flow angle remains the only useful direction. The formula for α is therefore modified such as to yield the flow angle in the degenerate case (Eq. 2.23). Inserting this value into Eq. (2.13) returns the flow speed.

Since entropy waves do not contribute to the detection of a wave direction from two neighboring states, one might as well remove these from the analysis. Eliminating entropy variations not accompanied by pressure variations leads to a very simple formula for α :

$$\tan (2\alpha) = 2[u] [v] / ([u]^2 - [v]^2) \quad (2.24)$$

This equation has two solutions:

$$\tan \alpha_1 = [v] / [u] , \tan \alpha_2 = -[u] / [v] \quad (2.25a,b)$$

Here u and v are the x - and y -components of the flow velocity. The first angle α_1 indicates the direction normal to a shock wave, the second angle α_2 the normal to a shear wave. By removing the entropy variations—which were irrelevant—bifurcation has been introduced: it is not clear how to switch smoothly from one case to the other for general data. In this respect the analysis is still incomplete.

Knowledge of α enables a solution to be found of the problem of the interaction between the two states, called Q_L and Q_R , in the proper frame of reference, in particular, using the proper projected velocities. The generic formula to compute the flux of the interface between two fluid cells follows from the solution of the Riemann problem defined by the different states. Solving the Riemann problem, however, requires an iterative procedure, even when the ideal-gas law is assumed, which explains the emergence of several highly useful "approximate Riemann solvers", reviewed in [3] and [4]. Knowledge of V suggests a new approximate Riemann solver, with the algebra brought down to the absolute minimum:

$$\hat{f}(Q_L, Q_R) = \frac{1}{2} [(\hat{f}(Q_L) + \hat{f}(Q_R)) - |V| (Q_R - Q_L)] \quad (2.26)$$

The sign \wedge indicates that the fluxes are measured in the direction of the wave vector. If the states Q_L and Q_R can be connected by a single discontinuity, this formula recovers the flux that follows from the exact Riemann solution.

Less clear is how to compute a flux in the direction $\alpha + \pi/2$, i.e. normal to the wave vector. This flux, indicated by \hat{g} , is needed for compounding the fluxes in an arbitrary direction, in particular, in the direction normal to the interface separating cells L and R (see Figure 2.9). The simplest formula is

$$\hat{g}(Q_L, Q_R) = \frac{1}{2} \{ \hat{g}(Q_L) + \hat{g}(Q_R) \} \quad (2.27)$$

but this leads to central-differencing of the \hat{g} -fluxes in the final updating scheme and could be unstable. Numerical tests confirm this as will be seen. Davis [5] avoided this type of instability by averaging \hat{g} over 3 cells rather than 2, as in Eq. (2.27), according to an algorithm distinguishing 8 cases. Present experimentation is aimed at finding a simpler, yet robust algorithm using a minimal number of data.

The above analysis is not restricted to updating schemes of a particular order of accuracy. In fact, tests of the numerical resolution of discontinuities are best carried out on the basis of a first-order upwind-differencing scheme, since the penalty on ignoring the direction of a discontinuity is greatest. Results for an oblique shock show the excessive smearing typical for a standard upwind scheme. In contrast, a shock aligned with the grid has only 1 to 2 cells across.

For the actual computations a scheme with second-order accuracy is needed (one of the so-called κ -schemes tested in [6]); this is presently being tested. The time-marching experimentation will be carried out with new explicit methods developed in parallel by some other doctoral students in the department. These combine a local but matrix-valued preconditioner with a Runge-Kutta-type updating scheme that hides a low-pass filter. Such a marching algorithm is needed for a successful multigrid strategy, to be added later. Both the preconditioner and the Runge-Kutta scheme depend crucially on the availability of directional information such as the angle α derived above. The choice of the marching scheme, viz. explicit rather than implicit, is motivated by the availability of vector computers, for which such schemes are pre-eminently suited.

2.3 Numerical Results

The numerical work was started by developing a set of grids on which to carry out the numerical computations. The logical first choice was a cartesian grid positioned along the wedge face extending from the nose back (Figure 2.10). However, once blowing is applied at the nose it is anticipated that the effective body shape will become more blunt and the shock may stand out off from the body and thus fall off this grid. Moreover, since the nose area is anticipated to be a critical area, a local concentration of points may prove worth while. With this in mind a standard polar grid and a C-type grid were developed (Figs. 2.11 and 2.12). The C-type grid in this case is the result of taking a regular C grid and letting the radius of curvature go to zero at the nose. This creates a set of triangles at the nose which should not be a problem with a Godonov-type finite-volume scheme. The C-type grid (as is the cartesian grid) is created by laying out points along the body and then constructing, row by row, nearly orthogonal cells with specified wall heights. By controlling these wall heights, one can expand or contract parts of the grid at will (i.e. concentrate points in a specific area).

In order to study various numerical effects, a series of test problems are derived from the full problem. The test problem considered first is the resolution of a shock due to a wedge with a 10° half angle in Mach 5 flow. The numerical calculations are carried out on a cartesian grid positioned along the wedge face. This results in a shock at an angle of about 9.5° relative to the lateral lines of the grid (exact solution). Initially, a first-order upwind scheme was tested using a Harten-Lax-Roe approximate Riemann solver for each dimension separately.

$$f(Q_L, Q_R) = \frac{1}{2} \{ [f(Q_L) + f(Q_R)] - |V_x|(Q_R - Q_L) \} \quad (2.28a)$$

$$g(Q_T, Q_B) = \frac{1}{2} \{ [g(Q_T) + g(Q_B)] - |V_y|(Q_T - Q_B) \} \quad (2.28b)$$

where V_x and V_y are based on one-dimensional information:

$$V_x = ([Q], [f]) / ([Q], [Q]), \quad (2.29a)$$

$$V_y = ([Q], [g])/([Q], [Q]). \quad (2.29b)$$

This application of an essentially "one dimensional" scheme to two dimensions results in excessive smearing of the shock, as seen in Figs 2.13 and 2.14. Figure 2.13 is a contour plot of the density; the x-axis lies along the face of the wedge, the y-axis normal to it. The nose of the wedge is at the origin. Figure 2.14 is a 3-D plot of the density jump. Again the nose of the wedge is at the origin, but now the y-axis lies along the face of the wedge, the x-axis normal to it. The x-y plane is the computational grid and the magnitude of the density is plotted normal to it along the z axis.

Next the first-order code was extended to calculate the cell interface fluxes based on fluxes measured normal to and parallel to the wave. The flux normal to the wave is described by the formula

$$\hat{f}(Q_R, Q_L) = \frac{1}{2} \{ [\hat{f}(Q_R) + \hat{f}(Q_L)] - |V|(Q_R - Q_L) \} \quad (2.30)$$

With V obtained from Eqs. (2.13 - 2.22), the flux tangent to the wave is found by the simple averaging procedure, Eq. (2.27). This results in an unstable scheme. The calculation was started with an initial-value distribution similar to that of the exact solution. Figure 2.15 shows the distribution after 3 time steps. Figure 2.16 shows the distribution after 233 time steps when one cell pressure has become negative.

By adding dissipation along the wave, i.e. using

$$\hat{g}(Q_R, Q_L) = \frac{1}{2} \{ [\hat{g}(Q_R) + \hat{g}(Q_L)] - |V|(Q_R - Q_L) \} \quad (2.31)$$

the scheme becomes stable but the lower quality of the non-rotated algorithm is recovered, as shown by the smeared shock in Fig. 2.17.

With this matter still unresolved a second-order upwind scheme was implemented. This produces sharper shocks to begin with, since it is assumed that the distribution of state quantities in

each cell is linear rather than uniform, as for the first-order scheme. The gradient of this distribution in each cell is obtained by central differencing, e.g.

$$\left(\frac{\partial u}{\partial x}\right)_j = \frac{\Delta_{j-1/2} u + \Delta_{j+1/2} u}{2\Delta x}, \quad (2.32)$$

but this value is "limited" in order to prevent numerical oscillations. It turns out that small oscillations nevertheless remain present; these are sensitive to the strength of the limiter as well as to the obliqueness of the shock with respect to the grid.

The limiter used for the results of Fig. 2.18 is the weakest possible one, due to Van Leer [7]:

$$\left\{\left(\frac{\partial u}{\partial x}\right)_j\right\}_{\text{limited}} = \begin{cases} \frac{1}{\Delta x} & \text{minmod} \left(2\Delta_{j-1/2} u, \frac{\Delta_{j-1/2} u + \Delta_{j+1/2} u}{2}, 2\Delta_{j+1/2} u \right) \\ & \text{if } \text{sgn}(\Delta_{j-1/2} u) = \text{sgn}(\Delta_{j+1/2} u) \\ 0 & \text{otherwise} \end{cases} \quad (2.33)$$

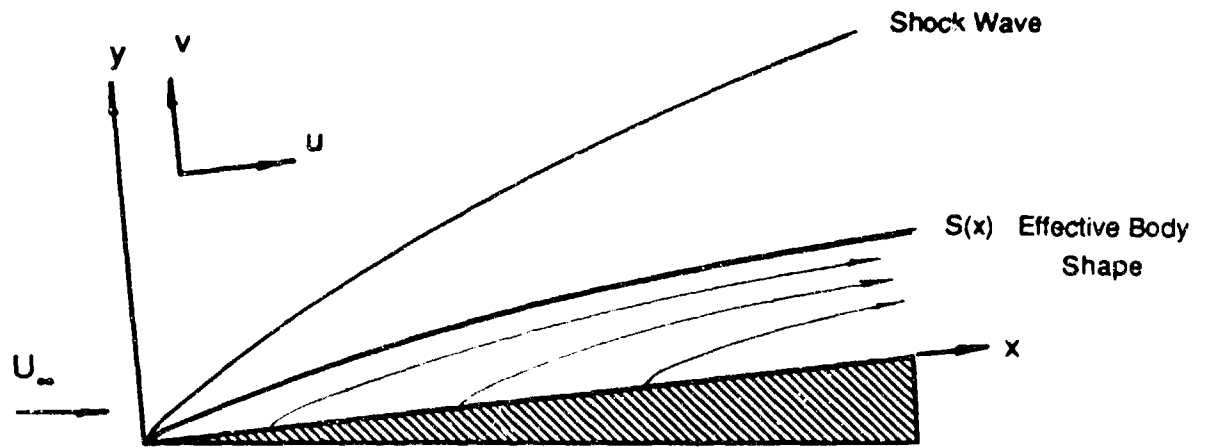
For Fig. 2.19 the strongest possible limiter was used:

$$\left\{\left(\frac{\partial u}{\partial x}\right)_j\right\}_{\text{limited}} = \begin{cases} \frac{1}{\Delta x} & \text{minmod}(\Delta_{j-1/2} u, \Delta_{j+1/2} u) \\ & \text{if } \text{sgn}(\Delta_{j-1/2} u) = \text{sgn}(\Delta_{j+1/2} u) \\ 0 & \text{otherwise} \end{cases} \quad (2.34)$$

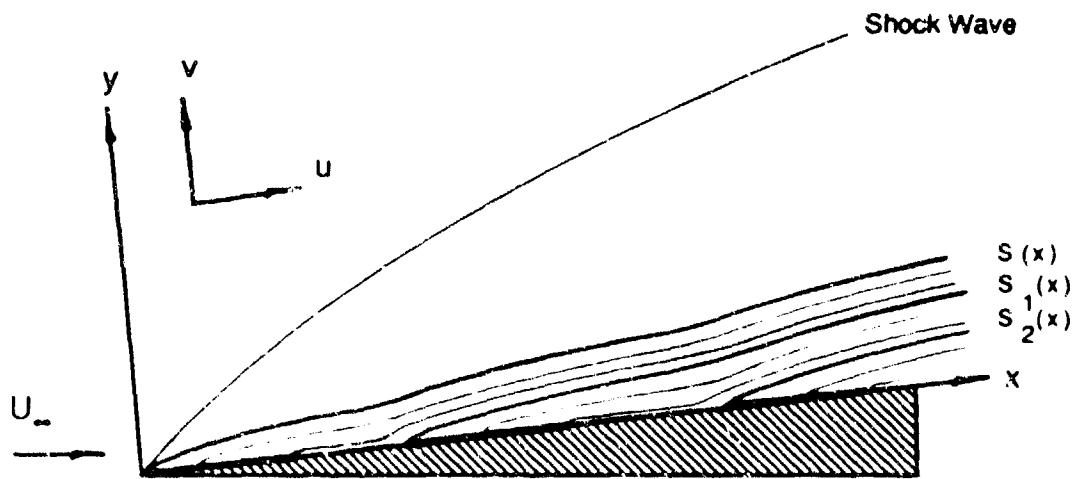
still leaving some oscillations. Adjusting the mesh ratio $\Delta y/\Delta x$ such that the shock runs diagonally across the grid (see Fig. 2.20) removes almost all oscillations when the limiter in Eq. (2.34) is used. Further experimentation is needed to ensure that the combination of flux formulas and gradient limiter gives a monotone shock profile regardless of the mesh ratio.

References

- [1] Cole, J. D. and Aroesty, "The Blowhard Problem-Inviscid Flows with Surface Injection," Memorandum RM-5196-ARPA, The Rand Corporation, April 1967.
- [2] van Leer, B., "The Computation of Steady Solutions to the Euler Equations: A Perspective," introductory review for the GAMM Workshop on Numerical Simulation of Compressible Euler Flows, 10-13 June 1986, Rocquencourt, France.
- [3] Harten, A., Lax, P.D., and van Leer, B., "Upstream Differencing and Godunov-type Schemes for Hyperbolic Conservation Laws," SIAM Rev. **25** (1983), pp. 35-61.
- [4] van Leer, B., Thomas, J.L., Roe, P. L., and Newsome, R.W., "A Comparison of Numerical Flux Formulas for the Euler and Navier-Stokes Equations," AIAA Paper AIAA-87-1104-CP.
- [5] Davis, S.F., "A Rotationally Biased Upwind Difference Scheme for the Euler Equations," J. Comp. Phys. **56** (1984), pp. 65-92.
- [6] Anderson, W.K., Thomas, J.L., and van Leer, B., "Comparison of Finite-Volume Flux-Vector Splittings for the Euler Equations," AIAA J. **24** (1986), pp. 1453-1480.
- [7] van Leer, B., "Towards the Ultimate Conservative Difference Scheme. II. Monotonicity and Conservation Combined in a Second-Order Scheme," J. Comp. Phys. **14** (1974), pp. 361-370.



a) Distributed Blowing.



b) Strip Blowing. (Dark strips on wall indicate regions where gas is injected.)

FIG 2.1 SKETCHES OF DISTRIBUTED AND STRIP BLOWING FOR FLOW OVER A SLENDER WEDGE.

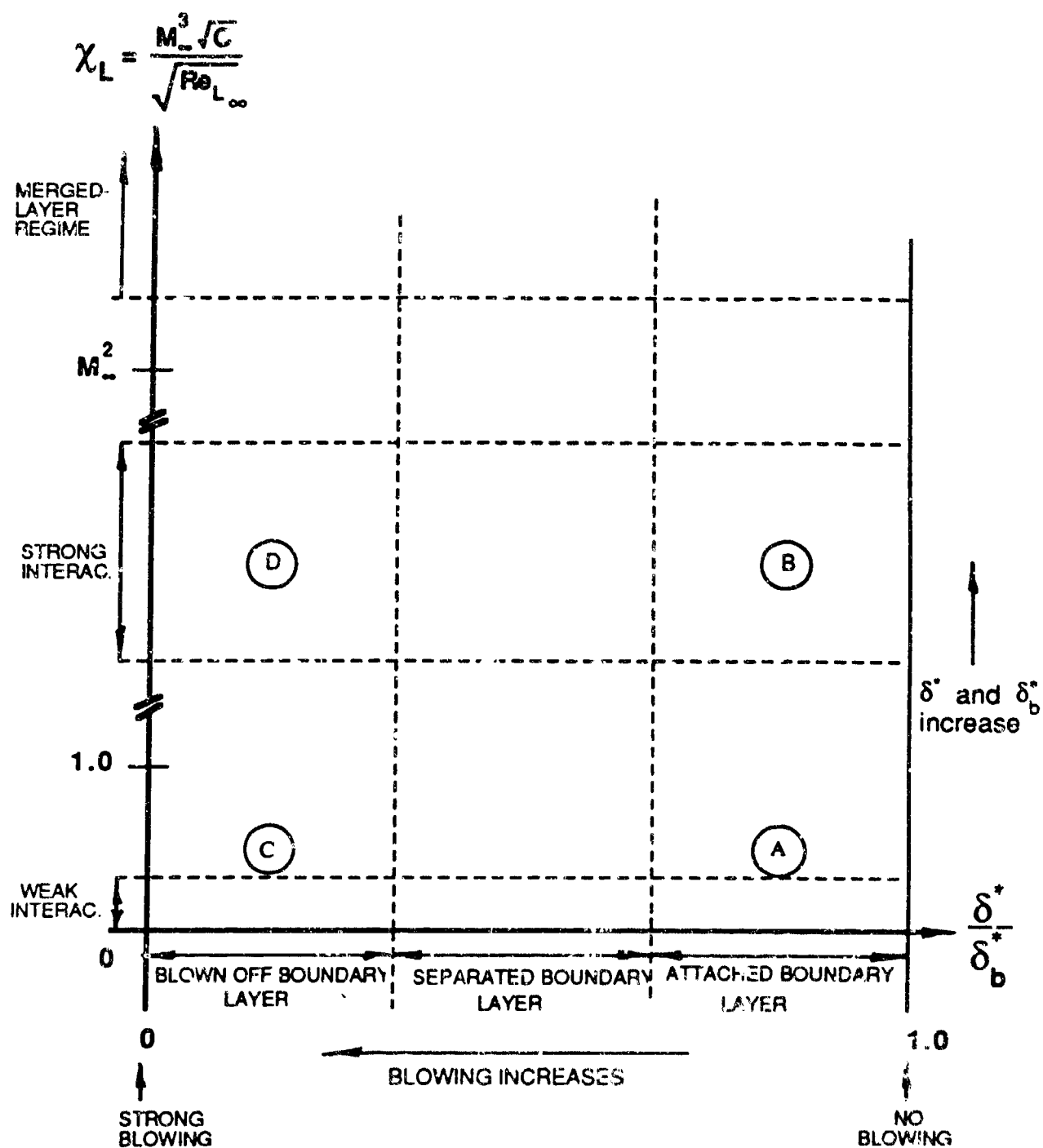


FIG 2.2 CHARACTERIZATION OF FLOWFIELD WITH BLOWING

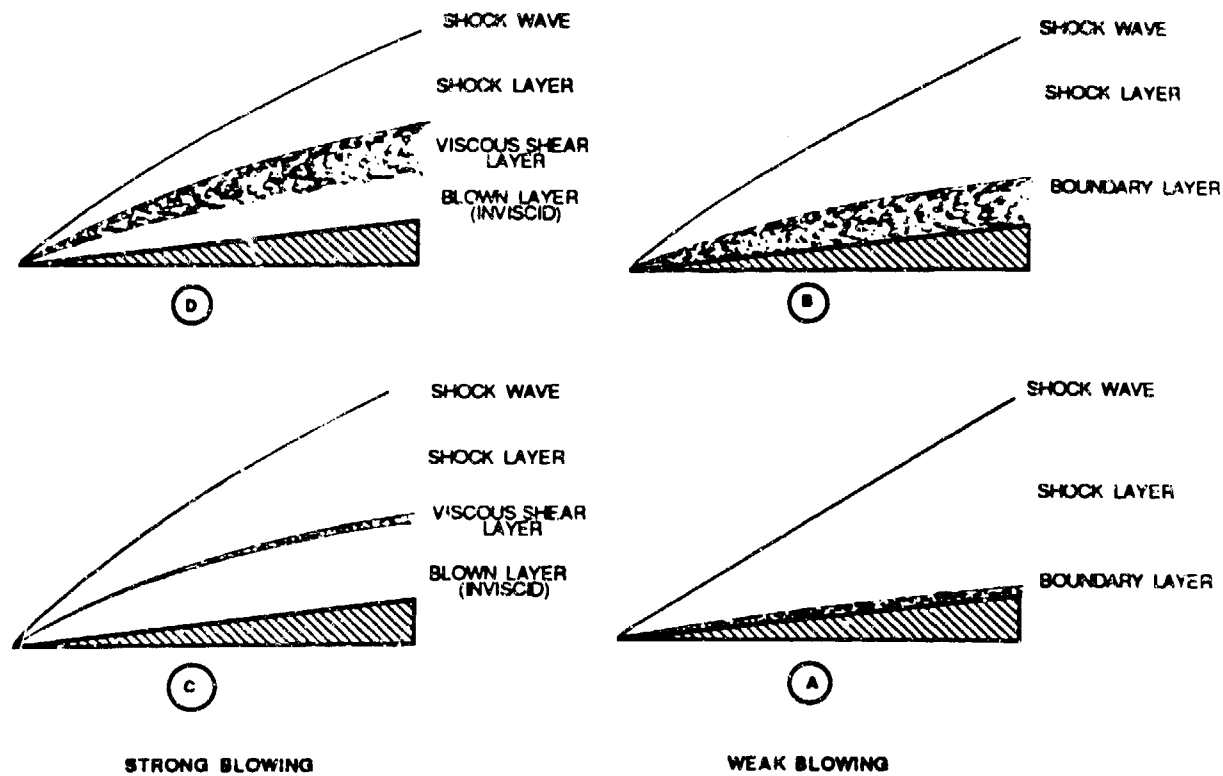


FIG 2.3 SKETCHES OF FLOWFIELDS
IN REGIMES INDICATED IN FIGURE (2.3).

COMPARISON OF BLOWHARD SOLUTIONS FOR
COMPRESSIBLE AND INCOMPRESSIBLE INNER LAYERS

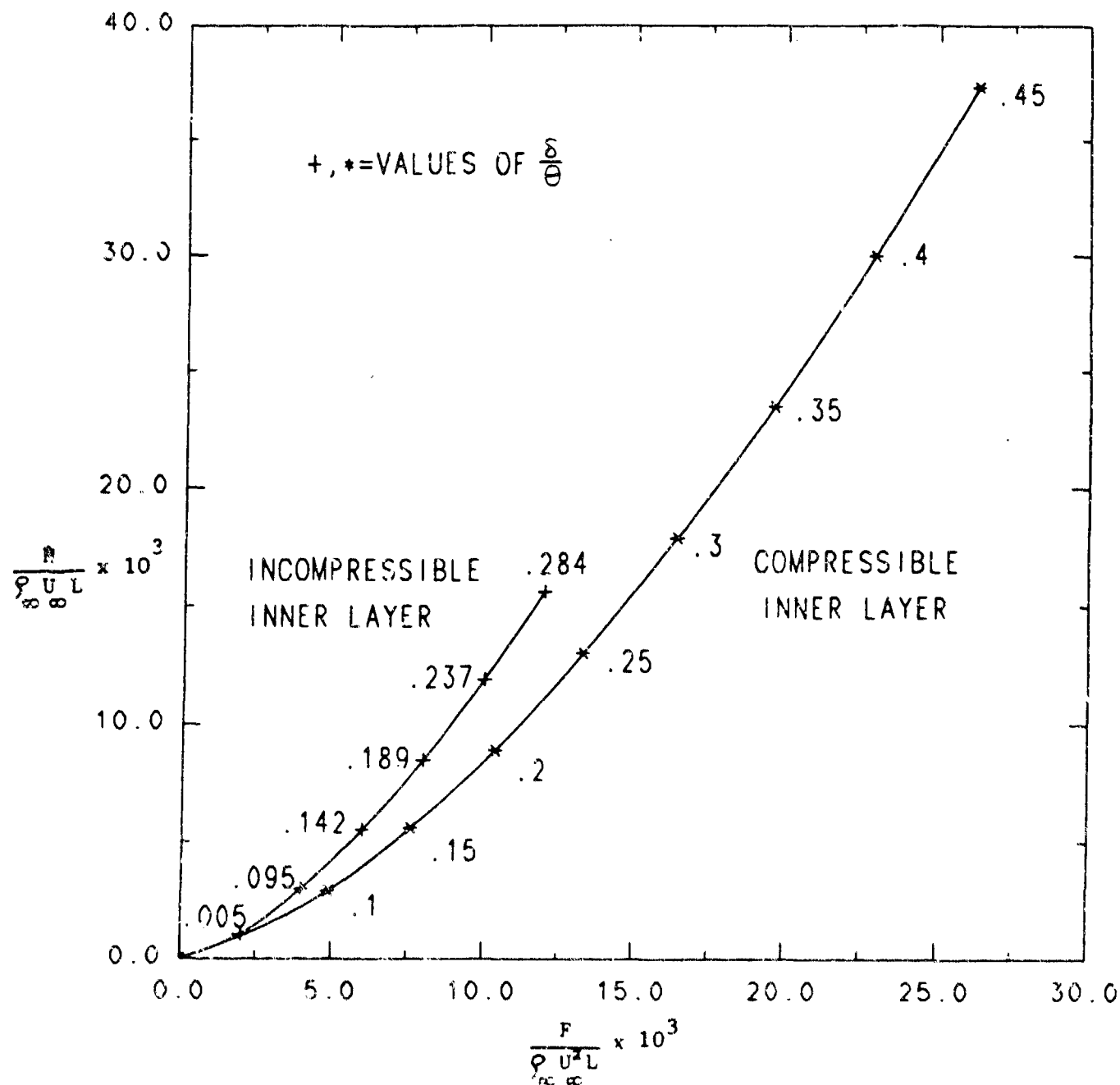


Fig. 2.4 INJECTED MASS FLOW RATE
VS.
BLOWING INDUCED NORMAL FORCE
 $M_{\infty}=20 \quad \theta=8^\circ$

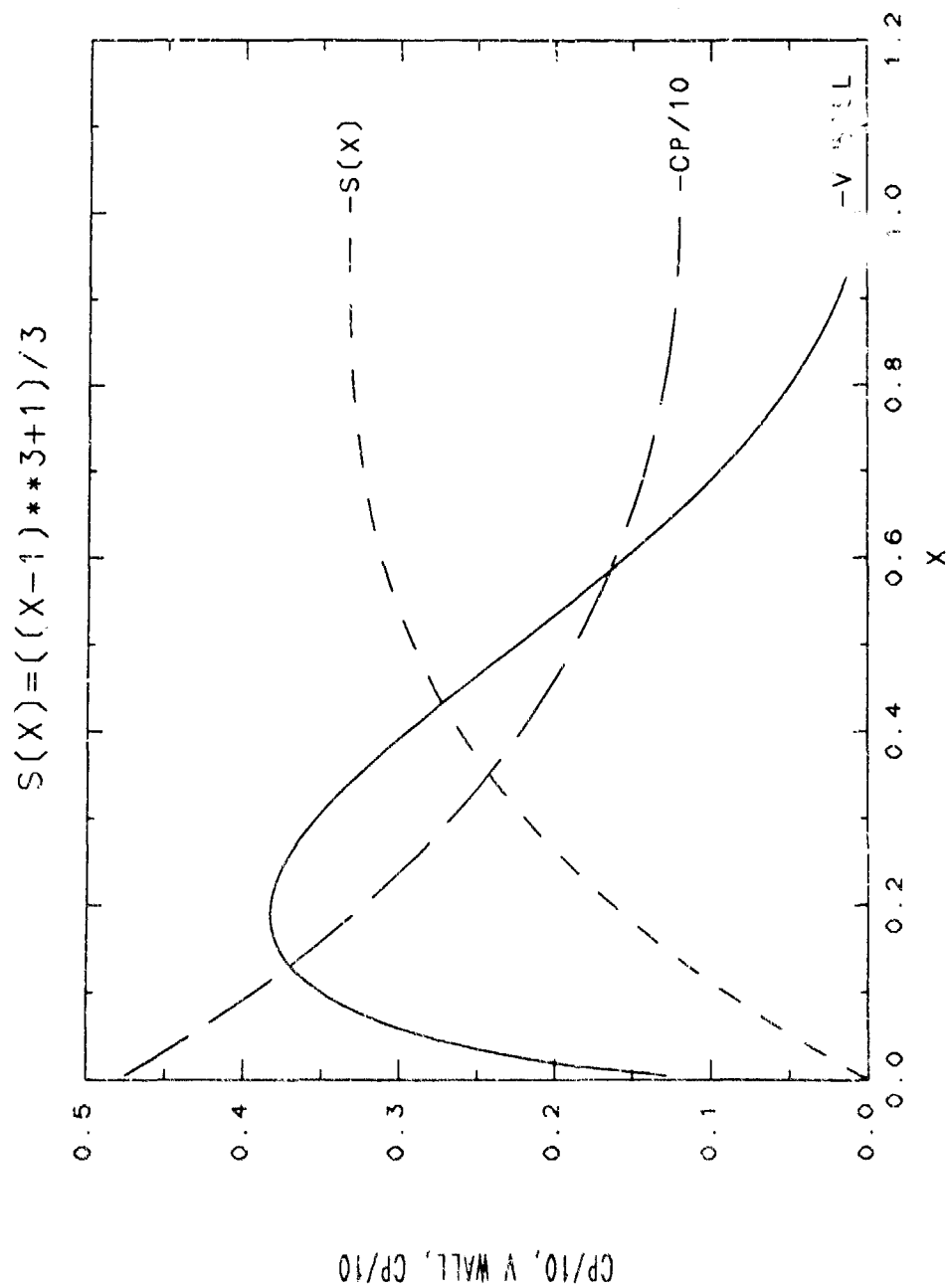


FIG 2.5 Plot of wall blowing velocity v_w and pressure coefficient C_p for indicated $s(x)$; compressible inner layer.

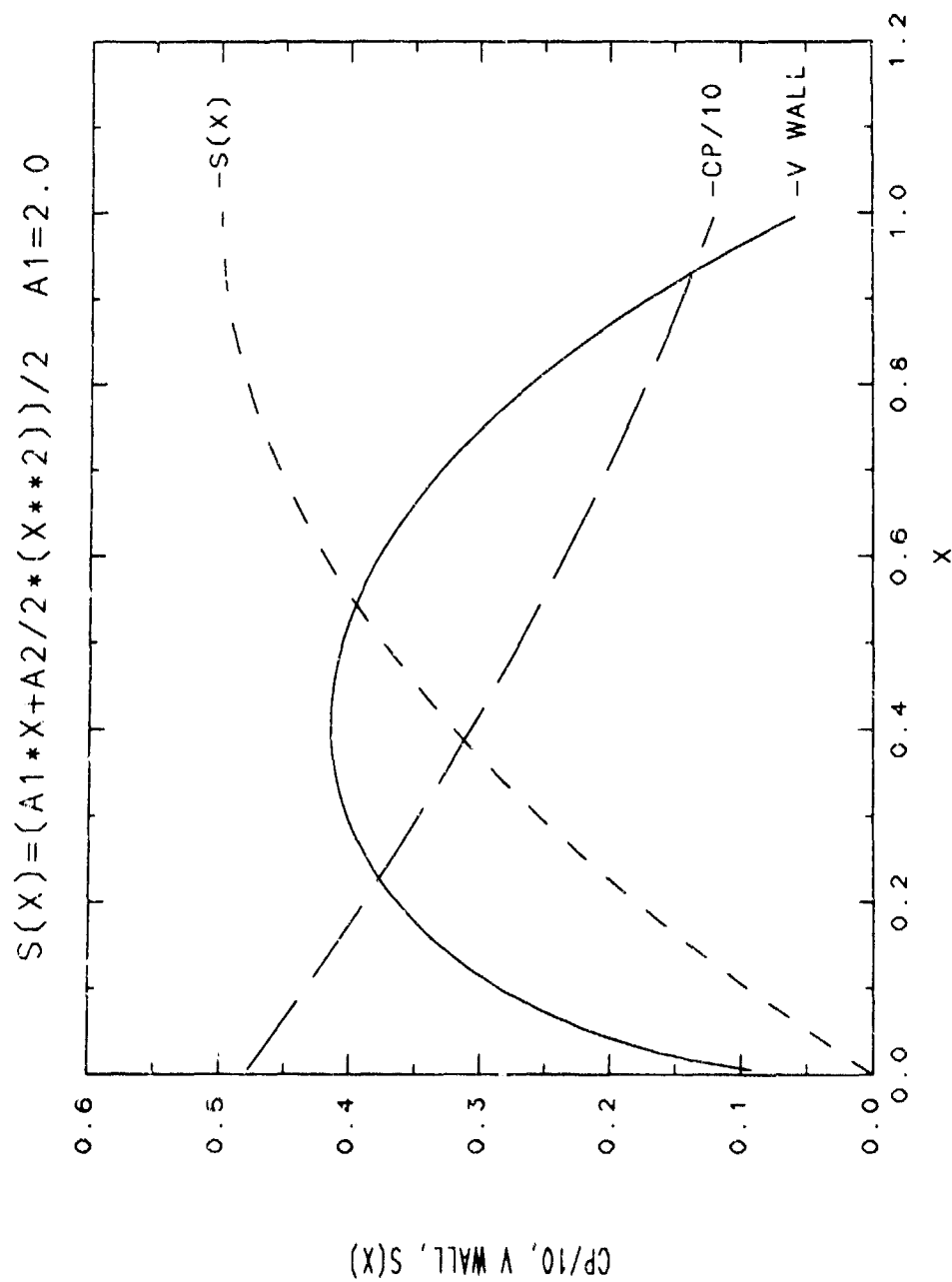
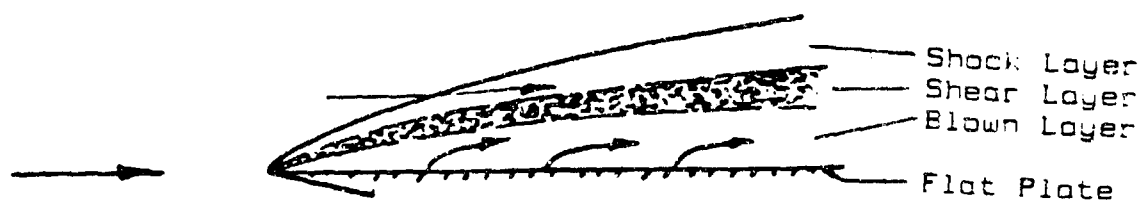


FIG 2.6 Plot of wall blowing velocity v_w and pressure coefficient C_p for indicated $s(x)$; compressible inner layer. $A_1 = 2 \quad A_2 = -2$

SKETCH OF FLOW-FIELD



SHEAR-LAYER VELOCITY AND TOTAL-ENTHALPY PROFILES

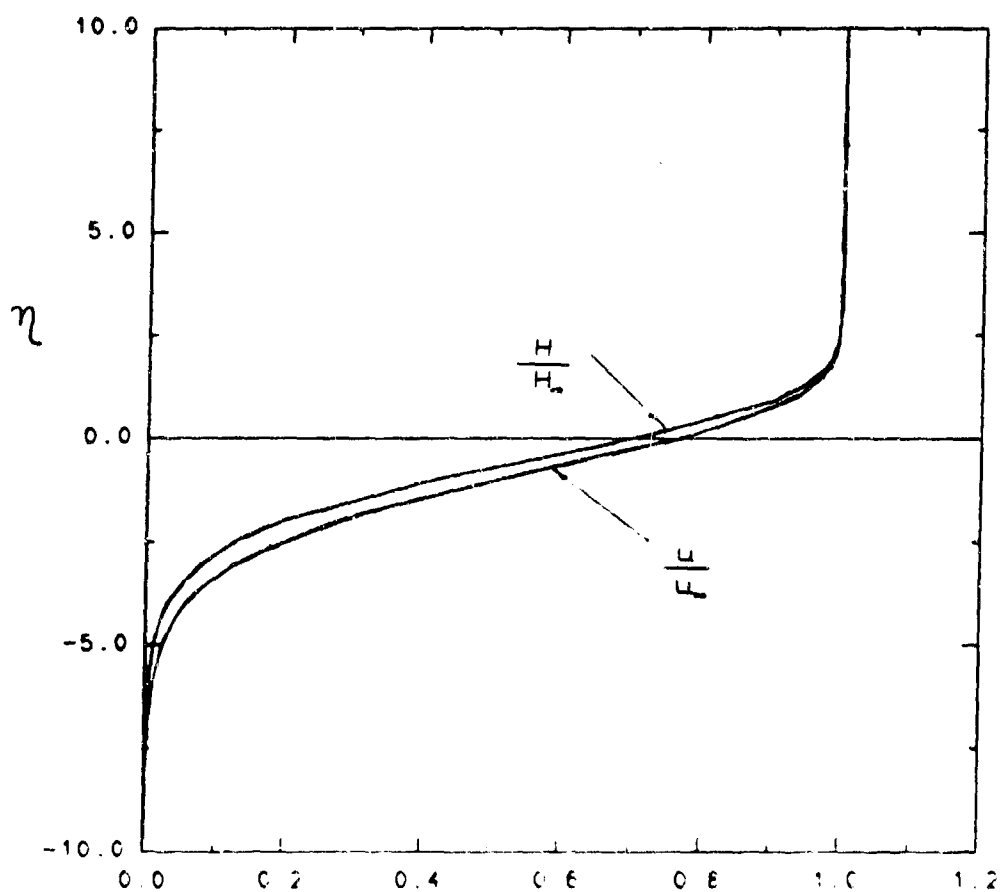


Fig. 2.7 Sketch of flow field and plots of shear layer velocity u/u_∞ and total enthalpy H/H_∞ profiles for case of strong blowing and non-negligible shear layer.

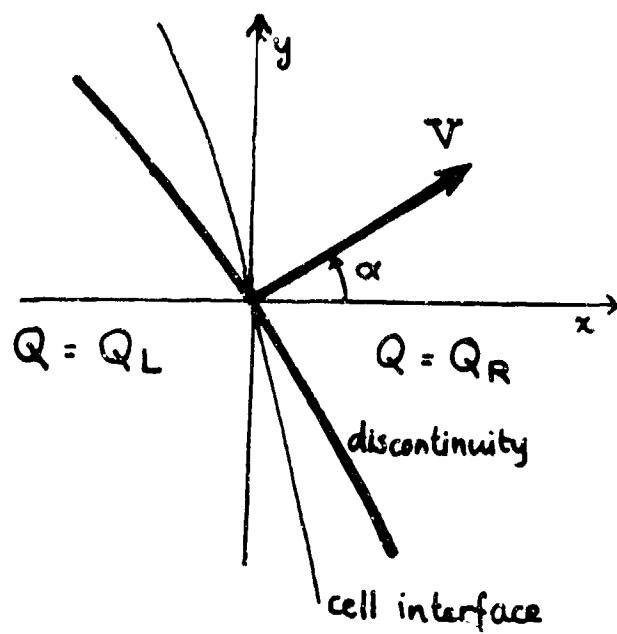


FIG 2.8 Definition of α and v

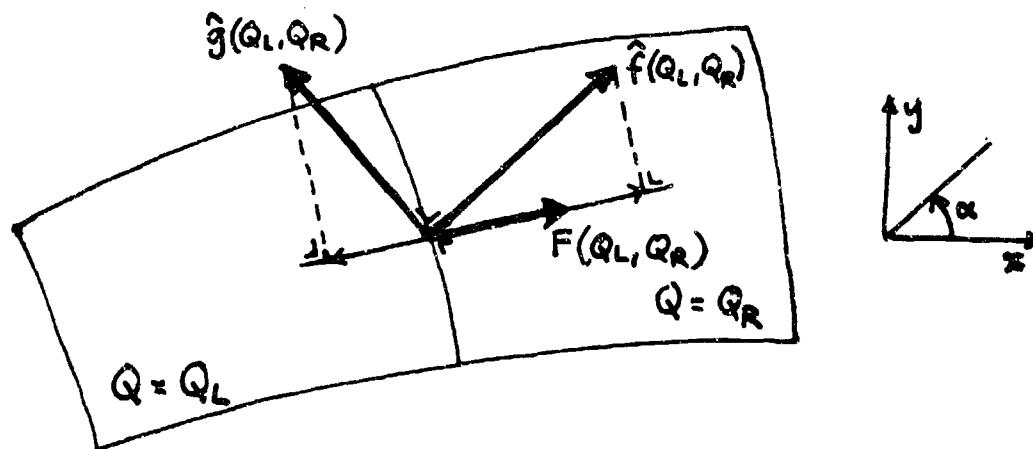


FIG 2.9 Sketch of adjoining cells; both \hat{f} and \hat{g} are needed to compute the flux F normal to the cell interface.

THETA=10 DEG.

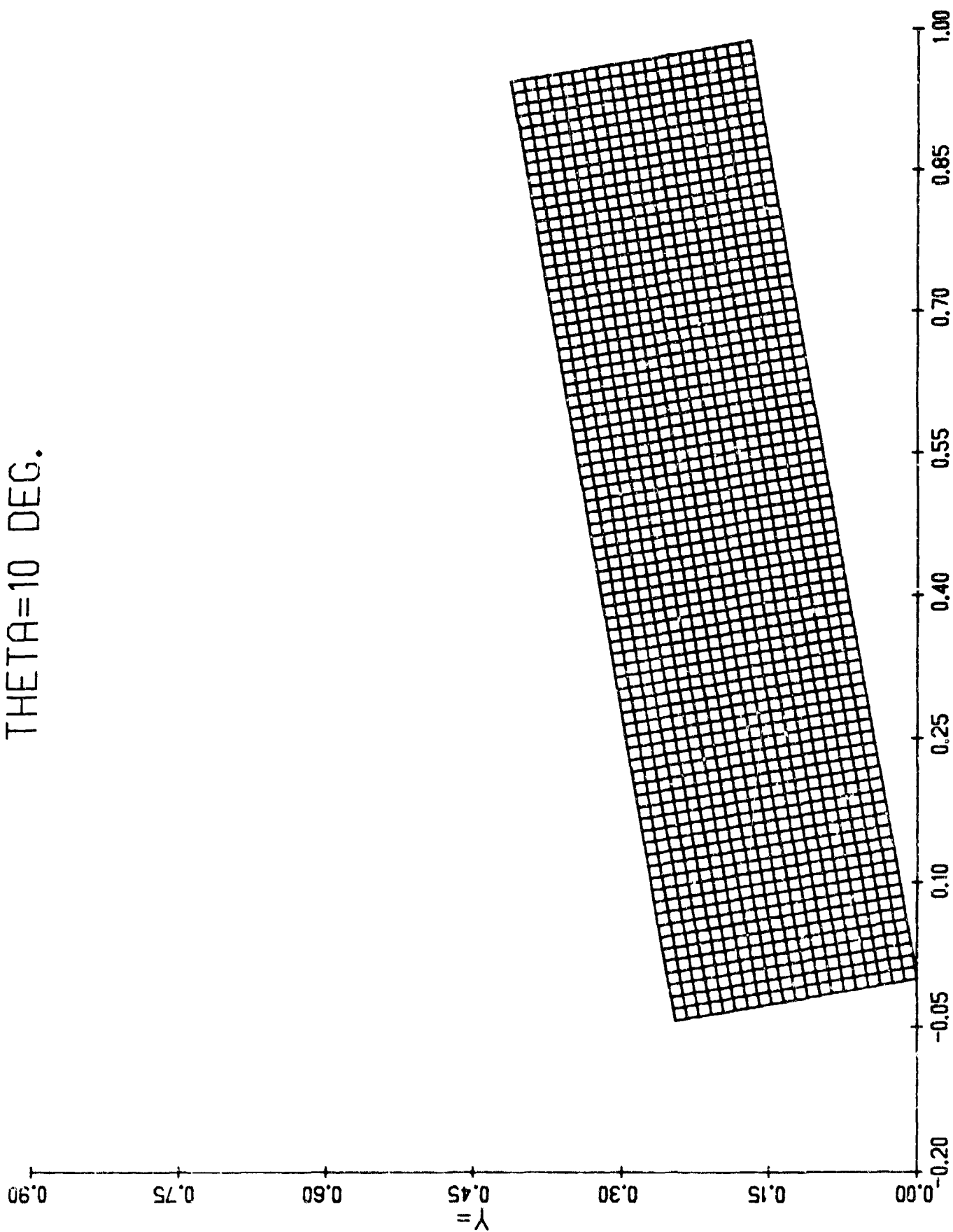


Fig. 2.10 Cartesian grid over wedge; $\theta = 10^\circ$.

THETA=10 DEG.

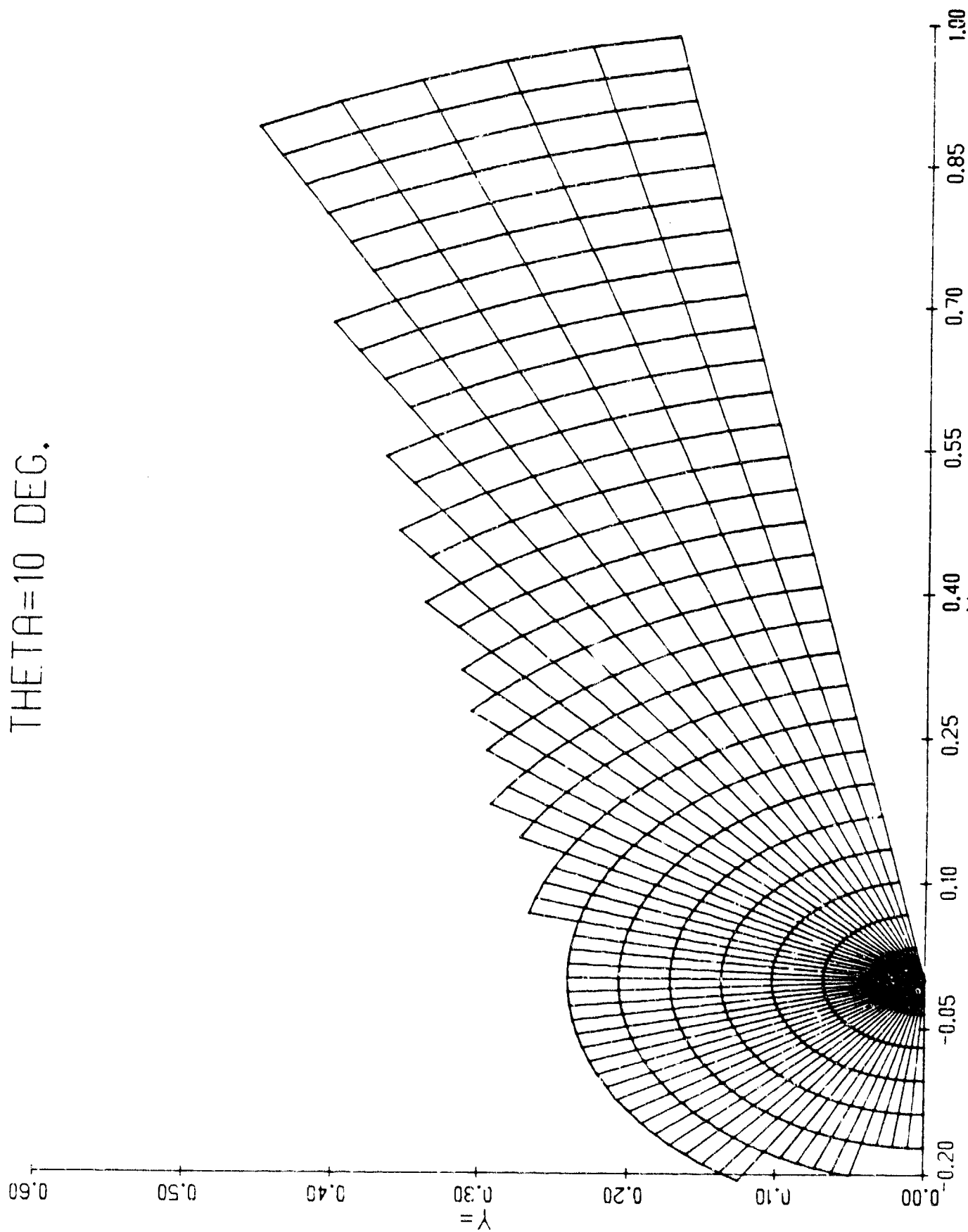


Fig. 2.11 Standard polar grid over wedge; $\theta = 10^\circ$,

THETA=10 DEG.

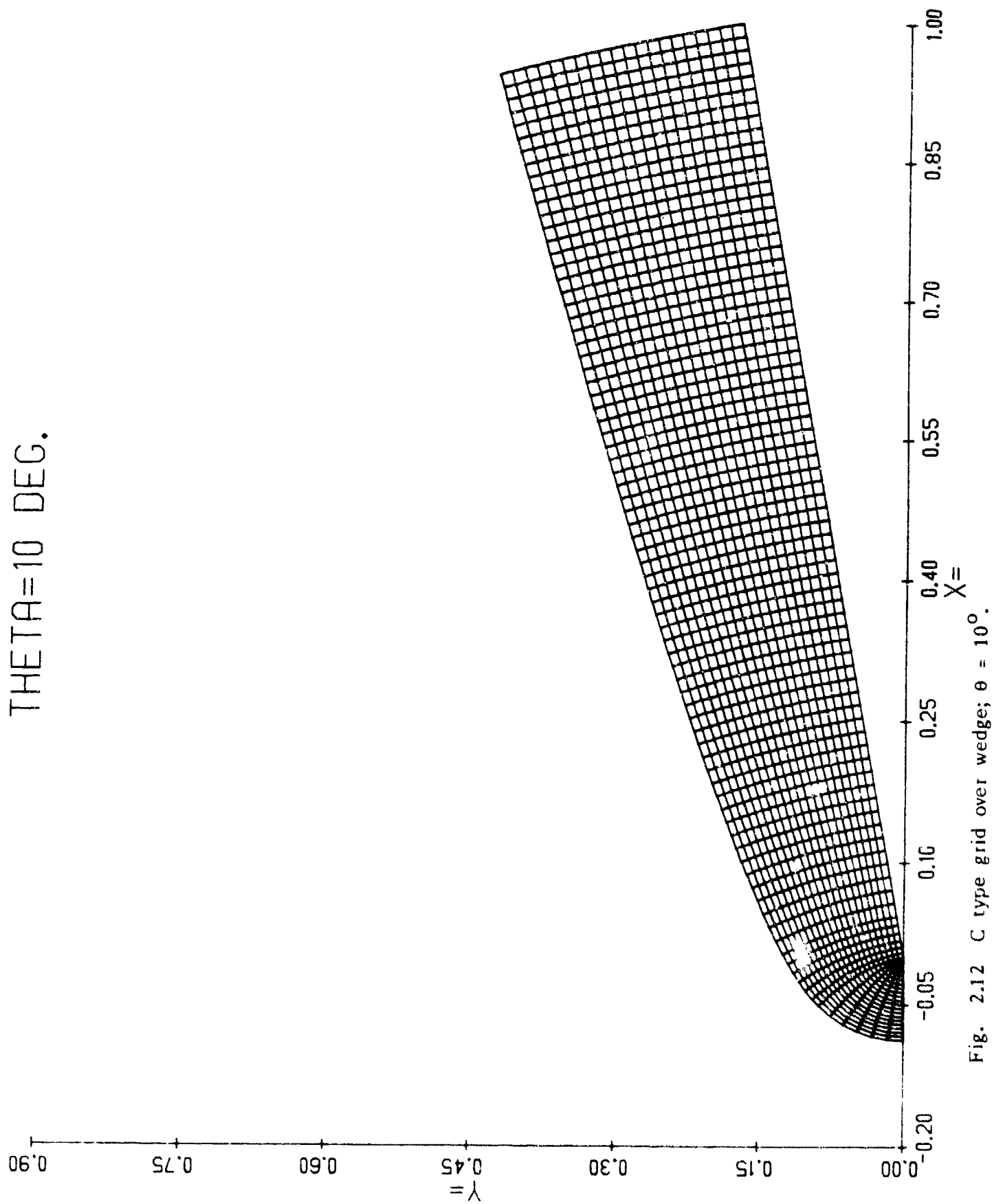


Fig. 2.12 C type grid over wedge; $\theta = 10^\circ$.

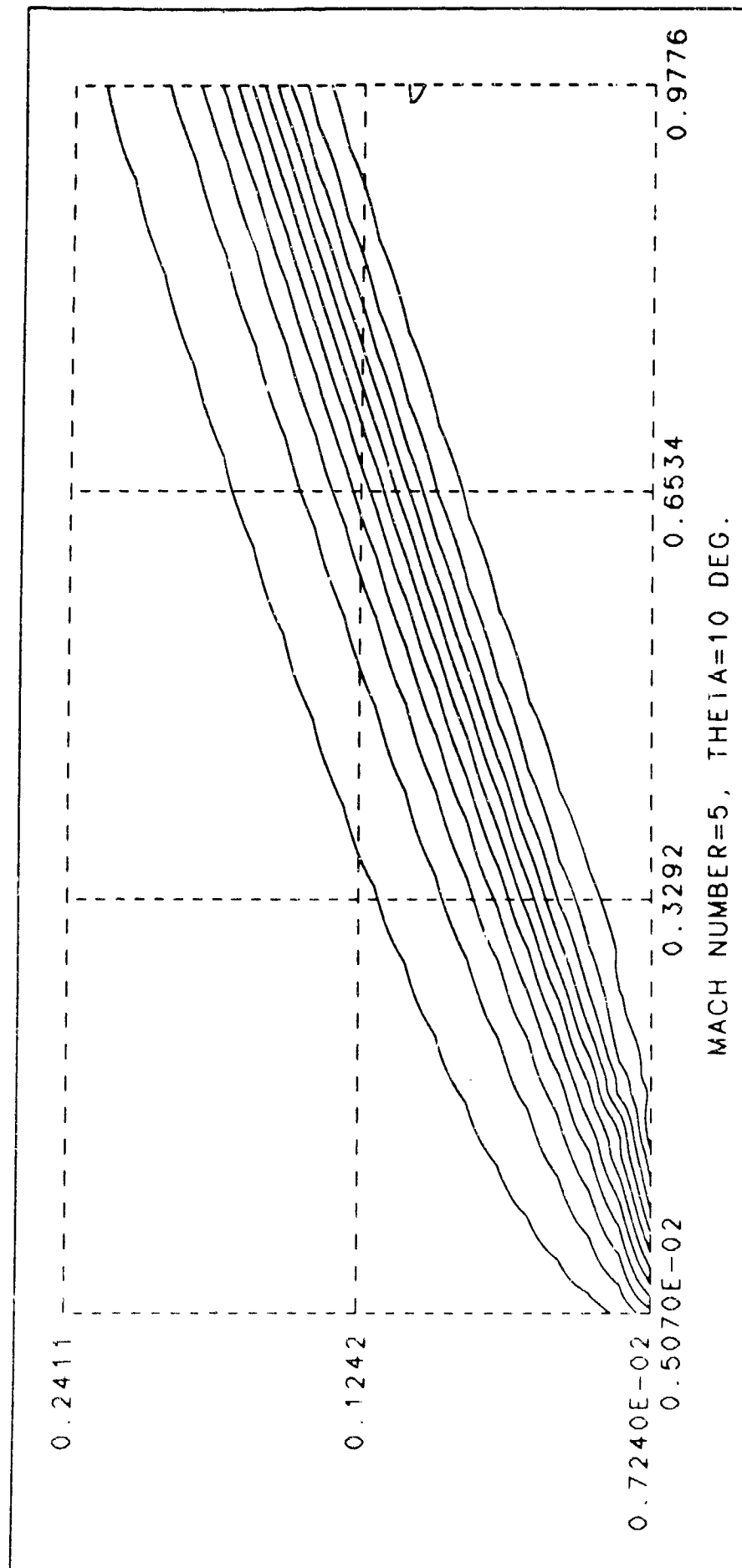


Fig. 2.13 Contour plot of the resulting density distribution when the Harten-Lax-Roe approximate Riemann solver is applied to each dimension separately. The X axis lies along the wedge face, and the Y axis is normal to the wedge face.

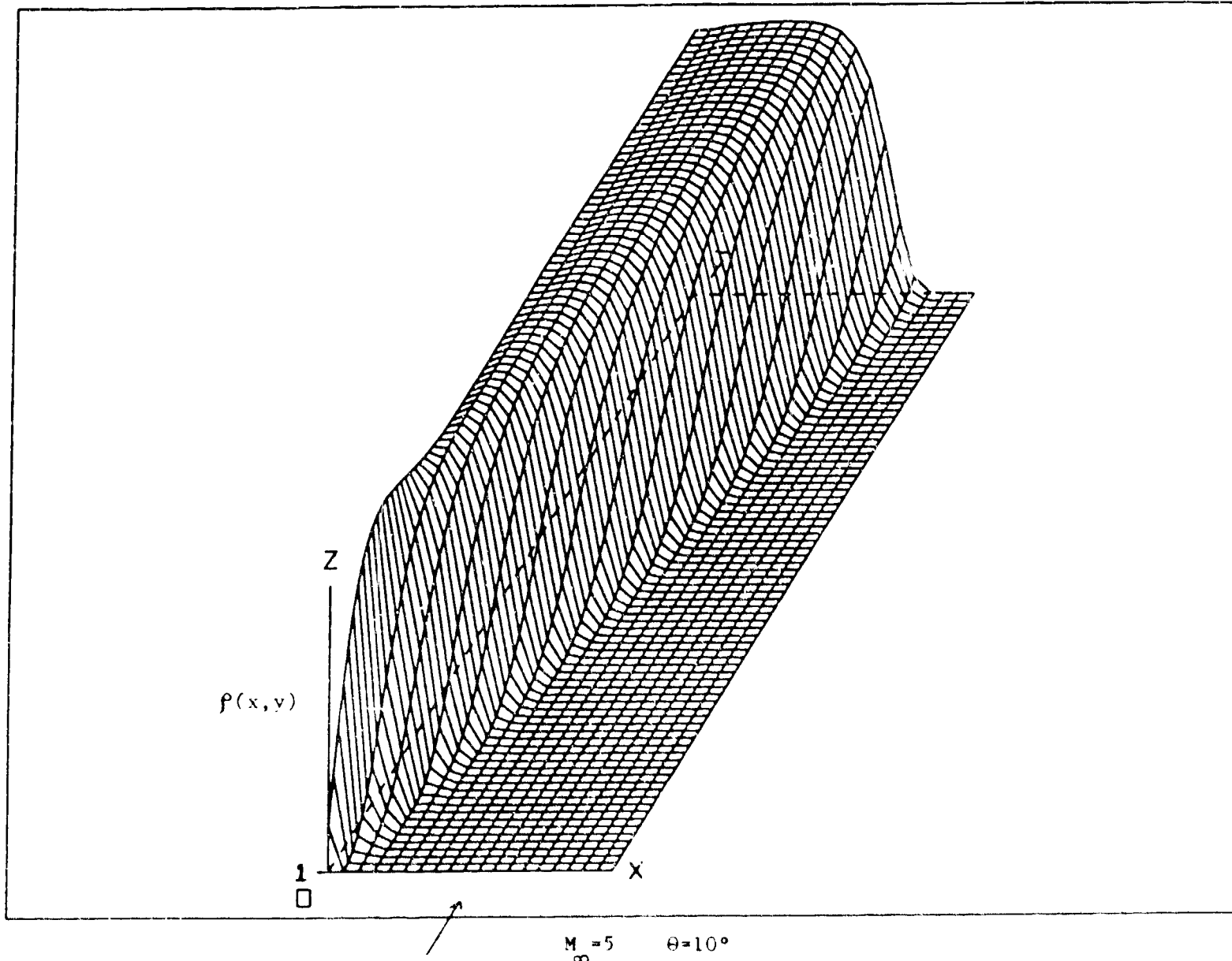


Fig. 2.14 Plot of the resulting density distribution when the Harten-Lax-Roe approximate Riemann solver is applied to each dimension separately. The Y axis lies along the wedge face, the X axis lies along the normal to the wedge face, and the density is plotted along the Z axis.

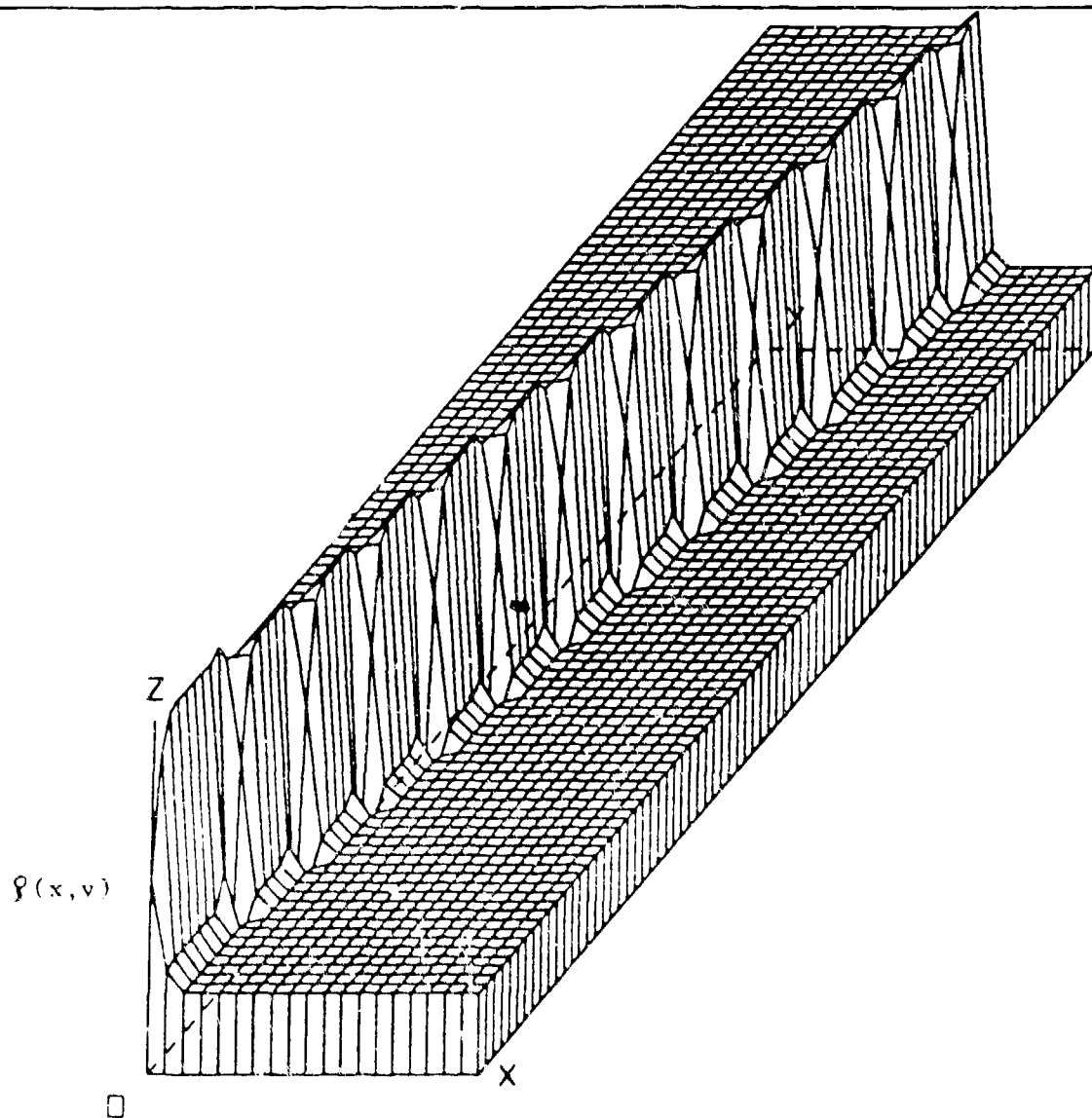


Fig. 2.15 Plot of the density for the case when numerical dissipation is added only normal to the wave. The scheme has been stopped after 3 time steps to show the onset of instability.

$$M_{\infty} = 5 \quad \theta = 10^\circ$$

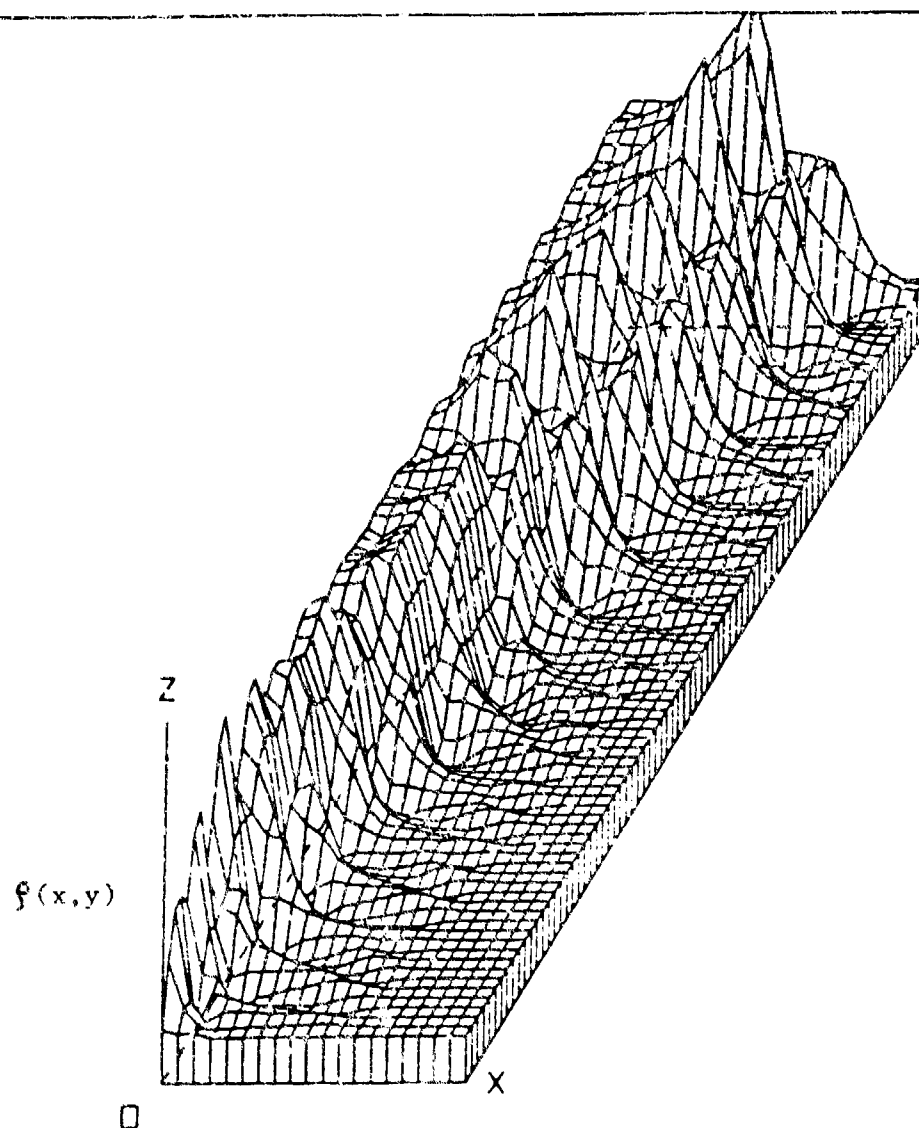


Fig. 2.16 Plot of the density for the case when numerical dissipation is added only normal to the wave. The pressure went negative after 233 time steps.

$$M_{\infty} = 5 \quad \theta = 10^\circ$$

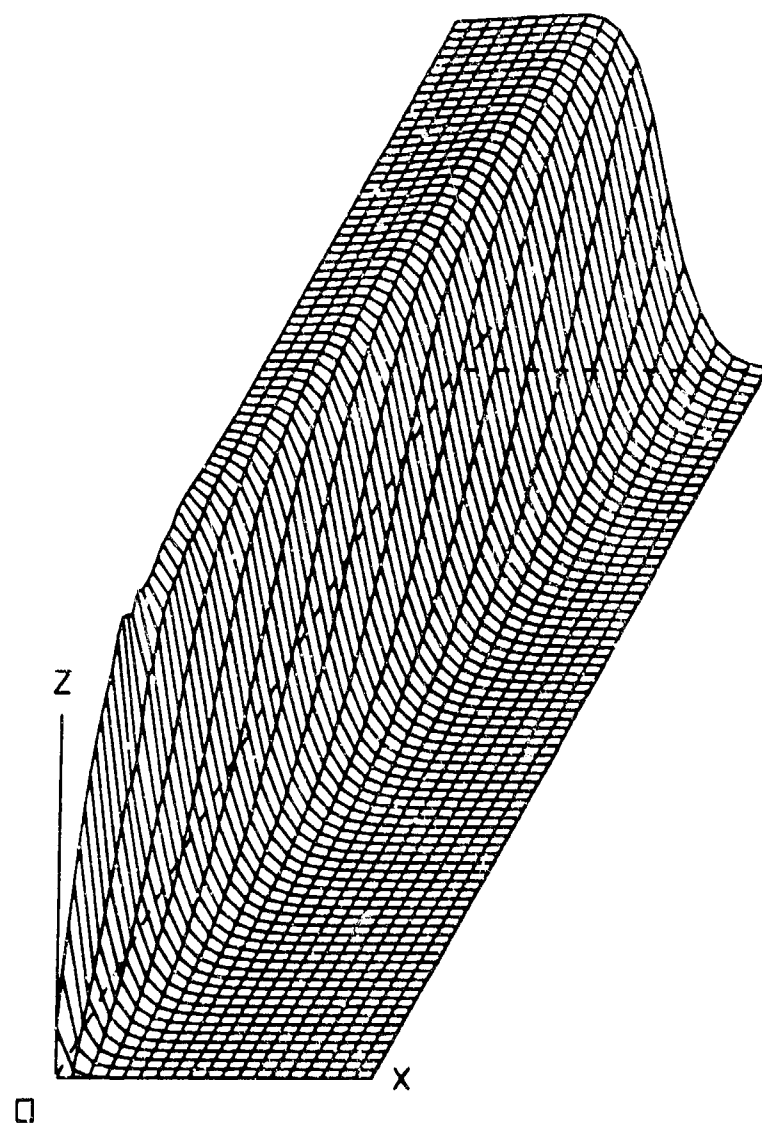


Fig. 2.17 Plot of the density for the case where numerical dissipation has been added both normal to and along the wave.

$$M_{\infty} = 5 \quad \theta = 10^\circ$$

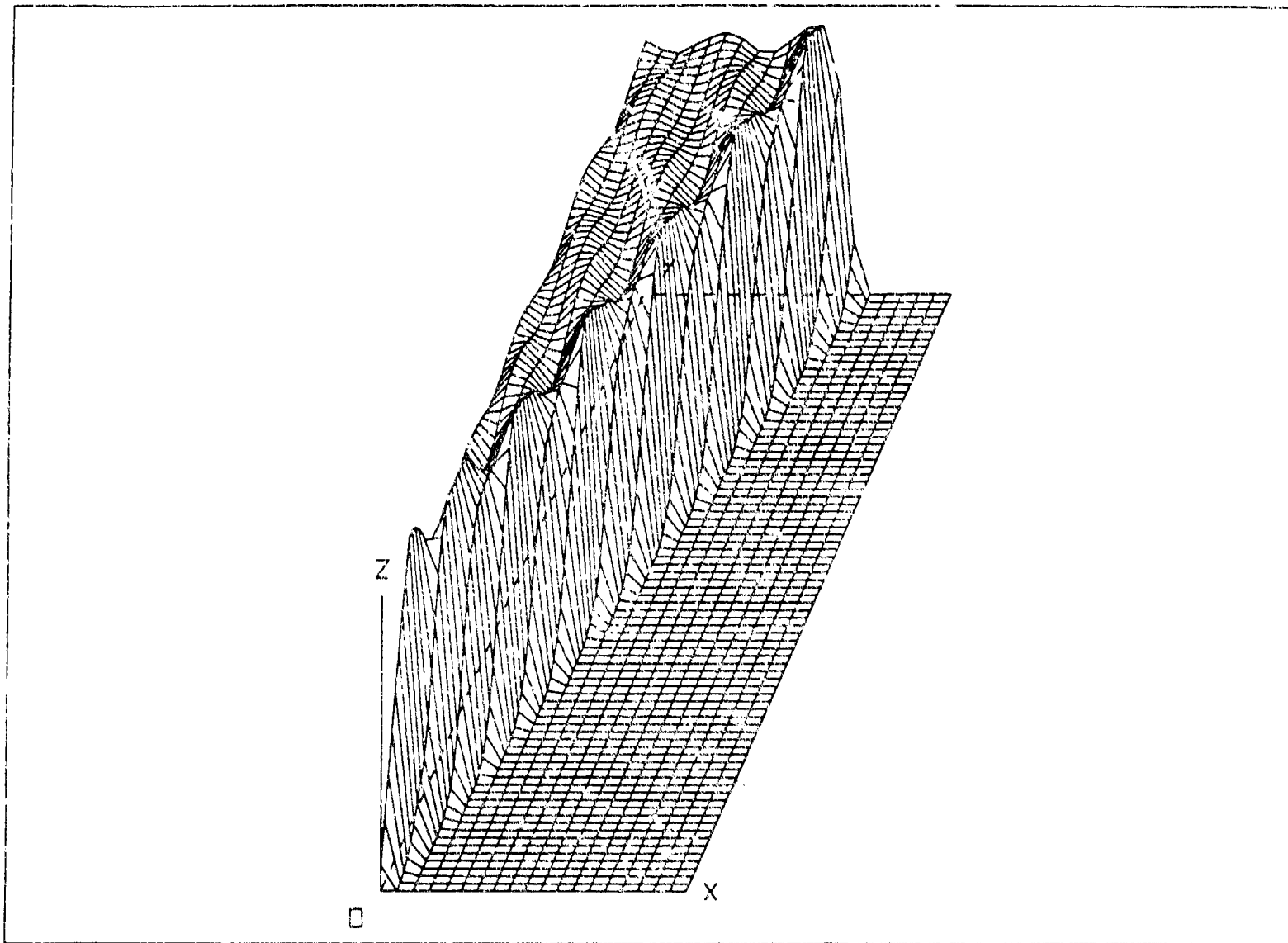


Fig. 2.18

Plot showing the magnitude of the density as found by the second order scheme using the flux limiter as in Eq. 2.33.

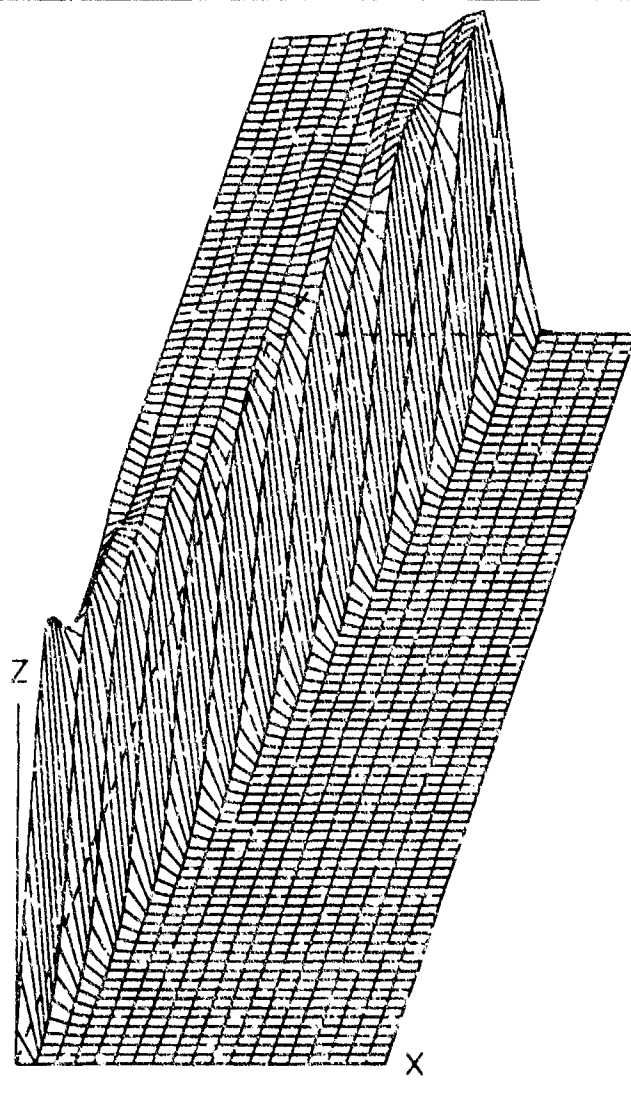


Fig 2.19

Plot showing the magnitude of the density as found by the second order scheme using the flux limiter as in Eq. 2.34.

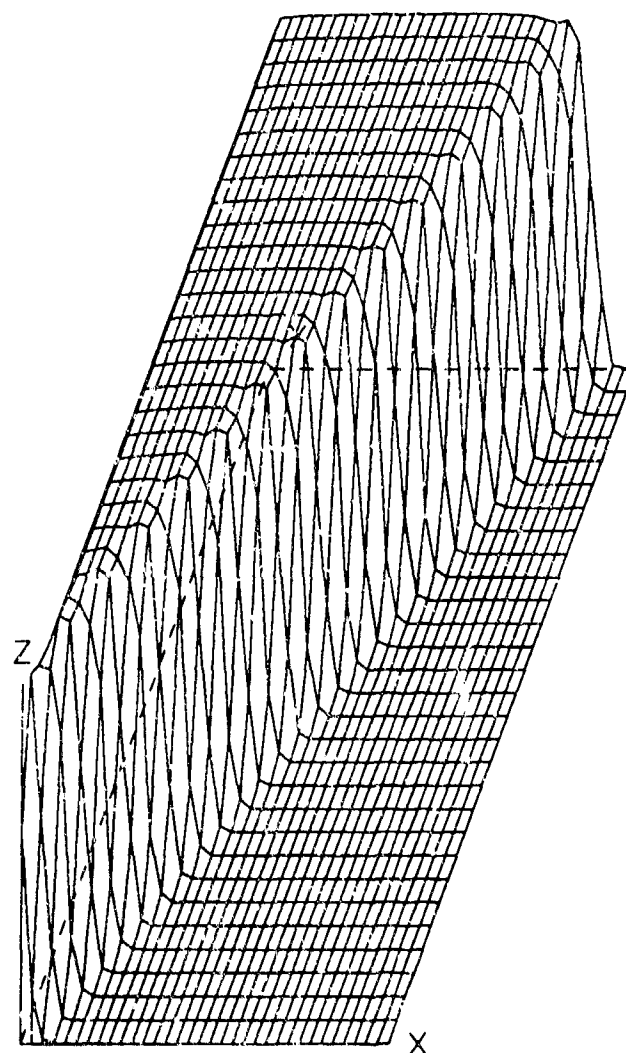


Fig. 2.20

Plot showing the magnitude of the density as found by the second order scheme using the flux limiter as in Eq. 2.34, but evaluated on a grid scaled such that the shock passes through each cell at a 45° angle relative to the cell walls $M_\infty = 5.9 = 10^0$

IV. Cumulative Chronological List of Written Publications

- 1) Gilbert, E.G., Howe, R. M., Lu, P., Vinh, N. X., "Trajectory Optimization of Earth-Launched Interceptors at Supercircular Speeds," Proceedings of Symposium on Innovative Science and Technology, Los Angeles, CA, 10-15 January 1988.
- 2) Howe, R.M., Gilbert, E.G., Lu, P., Shorr, G., Vinh, N.X., "Computation of Optimal Trajectories Using State-of-the-art Simulation Technology," Proceedings of the Conference on Aerospace Simulation, No. 3, Feb. 3-5, 1988, San Diego, CA.

V. Professional People Associated with the Research

Professor Thomas C. Adamson, Jr.
Professor Elmer G. Gilbert
Professor Robert M. Howe
Professor Arthur F. Messiter
Professor Bram van Leer
Professor Nguyen X. Vinh
Mr. Nelson Carter
Mr. Aharon Karou
Mr. Ping Lu
Mr. Michael Matarrese
Mr. Gil Shorr

VI. Interactions

a) Papers presented at meetings, conferences, seminars, etc.

1. Gilbert E. G., Howe, R. M., Lu, P., Vinh, N. X., "Trajectory Optimization of Earth-Launched Interceptors at Supercircular Speeds," Symposium on Innovative Science and Technology, Los Angeles, CA, January 10-15, 1988.
2. Howe, R.M., Gilbert, E.G., Lu, P., Shorr, G., Vinh, N.X., "Computation of Optimal Trajectories Using State-of-the-art Simulation Technology," Conference on Aerospace Simulation, No. 3, Feb. 3-5, 1988, San Diego, CA.
3. Howe, R.M., and Jahangir, E., "A Guidance Scheme for Homing Missiles Based on Attitude Control by a Single-Axis Thruster," Ninth Meeting of the Coordinating Group on Modern Control Theory, Feb. 3-4, 1988, Oakland University, Rochester, MI 48309.

b) Consultative and Advisory Functions

None

VII. New Discoveries, Inventions, or Patent Disclosures.

None

VIII. Additional Statements

None